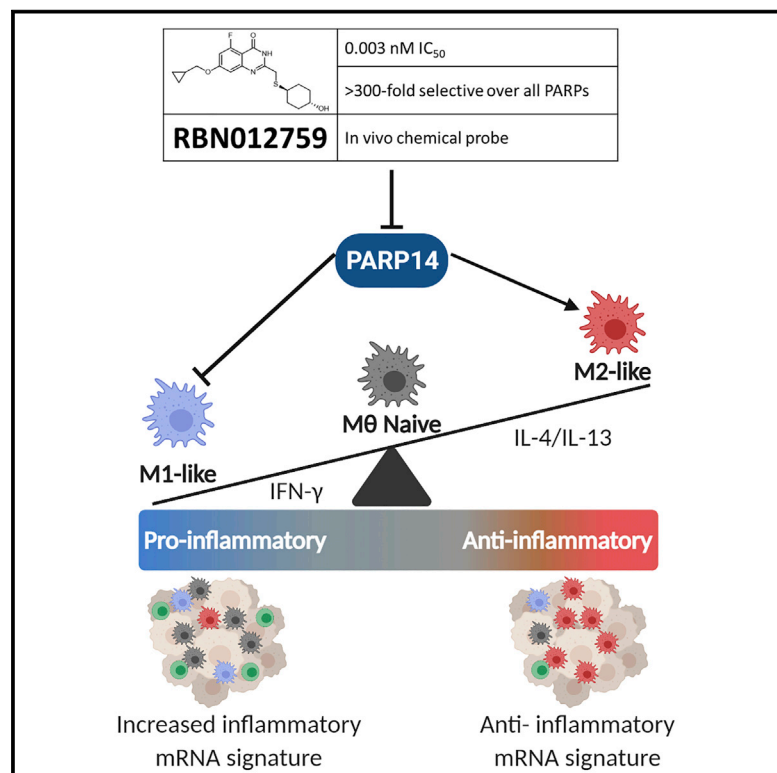


Cell Chemical Biology

A potent and selective PARP14 inhibitor decreases protumor macrophage gene expression and elicits inflammatory responses in tumor explants

Graphical abstract



Authors

Laurie B. Schenkel, Jennifer R. Molina, Kerren K. Swinger, ..., Victoria M. Richon, Heike Keilhack, Kevin W. Kuntz

Correspondence

kkuntz@ribontx.com

In brief

Schenkel et al. disclose the first highly potent and selective inhibitor of PARP14, RBN012759, an *in vitro* and *in vivo* chemical probe. RBN012759 reverses IL-4-driven protumor gene expression in macrophages and induces an inflammatory mRNA signature in primary human tumor explants, suggesting utility of PARP14 inhibitors for treating cancer.

Highlights

- The first highly potent and selective inhibitor of PARP14, RBN012759, is described
- The profile of RBN012759 enables its use as an *in vitro* and *in vivo* chemical probe
- RBN012759 reversed IL-4-driven protumor gene expression
- An inflammatory gene signature was activated with RBN012759 treatment

Article

A potent and selective PARP14 inhibitor decreases protumor macrophage gene expression and elicits inflammatory responses in tumor explants

Laurie B. Schenkel,^{1,3} Jennifer R. Molina,² Kerren K. Swinger,^{1,4} Ryan Abo,^{2,5} Danielle J. Blackwell,¹ Alvin Z. Lu,² Anne E. Cheung,^{2,6} W. David Church,¹ Kaiko Kunii,² Kristy G. Kuplast-Barr,² Christina R. Majer,¹ Elena Minissale,² Jan-Rung Mo,² Mario Niepel,² Christopher Reik,^{1,7} Yue Ren,¹ Melissa M. Vasbinder,¹ Tim J. Wigle,¹ Victoria M. Richon,^{1,2} Heike Keilhack,² and Kevin W. Kuntz^{1,8,*}

¹Department of Molecular Discovery, Ribon Therapeutics, Inc., Cambridge, MA 02140, USA

²Department of Biological Sciences, Ribon Therapeutics, Inc., Cambridge, MA 02140, USA

³MOMA Therapeutics, Cambridge, MA 02142, USA

⁴Xilio Therapeutics, Waltham, MA 02451, USA

⁵Obsidian Therapeutics, Cambridge, MA 02138, USA

⁶A2Empowerment, Arlington, MA 02474, USA

⁷Bain & Company, Boston, MA 02116, USA

⁸Lead contact

*Correspondence: kkuntz@ribontx.com

<https://doi.org/10.1016/j.chembiol.2021.02.010>

SUMMARY

PARP14 has been implicated by genetic knockout studies to promote protumor macrophage polarization and suppress the antitumor inflammatory response due to its role in modulating interleukin-4 (IL-4) and interferon- γ signaling pathways. Here, we describe structure-based design efforts leading to the discovery of a potent and highly selective PARP14 chemical probe. RBN012759 inhibits PARP14 with a biochemical half-maximal inhibitory concentration of 0.003 μ M, exhibits >300-fold selectivity over all PARP family members, and its profile enables further study of PARP14 biology and disease association both *in vitro* and *in vivo*. Inhibition of PARP14 with RBN012759 reverses IL-4-driven protumor gene expression in macrophages and induces an inflammatory mRNA signature similar to that induced by immune checkpoint inhibitor therapy in primary human tumor explants. These data support an immune suppressive role of PARP14 in tumors and suggest potential utility of PARP14 inhibitors in the treatment of cancer.

INTRODUCTION

PARPs (poly(ADP-ribose) polymerases) are a family of 17 enzymes known to regulate fundamental cellular processes, including gene expression, protein degradation, and multiple cellular stress responses (Vyas and Chang, 2014). PARPs utilize nicotinamide adenine dinucleotide (NAD⁺) to post-translationally modify substrates, including DNA, RNA, and protein, via transfer of a single ADP-ribose unit (mono-ADP-ribosylation or MARYlation) in the case of the PARP-monoenzyme subfamily, or chains of ADP-ribose units (poly-ADP-ribosylation or PARYlation) in the case of the PARP-polyenzymes (Cohen and Chang, 2018). PARP14 is a macrodomain-containing PARP-monoenzyme that was originally identified as *BAL2* (B aggressive lymphoma 2), a gene associated with poor outcome of diffuse large B cell lymphoma (Juszczynski et al., 2006; Aguiar et al., 2000, 2005). *PARP14* is an interferon-stimulated gene (ISG), whose mRNA expression is increased by all three types of interferons (Rusinova et al., 2013). It has been identified as a negative downstream regulator of interferon- γ (IFN- γ) and STAT1 transcription, and as a positive regulator of the interleukin-4 (IL-4) and STAT6 signaling cascade (Goenka et al., 2007; Mehrotra et al., 2011).

Based on the proposed opposing effects on IFN- γ - and IL-4-mediated gene expression, PARP14 has been implicated in macrophage polarization. Genetic PARP14 inactivation in macrophages skews them toward a pro-inflammatory IFN- γ -driven M1 phenotype while reducing the IL-4-driven M2 phenotype (Iwata et al., 2016). In line with these results, PARP14 knockout (KO) showed therapeutic effects in Th2 cytokine-driven models of allergic airway disease (Cho et al., 2013; Mehrotra et al., 2013).

Several PARP14 inhibitors have been previously disclosed, including compounds that bind the NAD⁺ pocket in the catalytic domain (Ekblad et al., 2015; Andersson et al., 2012; Peng et al., 2017; Upton et al., 2017; Yoneyama-Hirozane et al., 2017; Wang et al., 2014; lansante et al., 2015; Holechek et al., 2018), as well as those that bind the PARP14 macrodomains (Ekblad et al., 2018; Moustakim et al., 2018; Schuller et al., 2017). While in some cases the catalytic inhibitors inhibit PARP14 with biochemical half-maximal inhibitory concentration (IC₅₀) values in the sub-micromolar range, achieving significant PARP14 selectivity has remained challenging due to high sequence similarity among the PARP family NAD⁺ binding pockets and lack of access to a complete panel of sensitive, high-throughput PARP assays to fully evaluate selectivity (Thorsell et al., 2017;

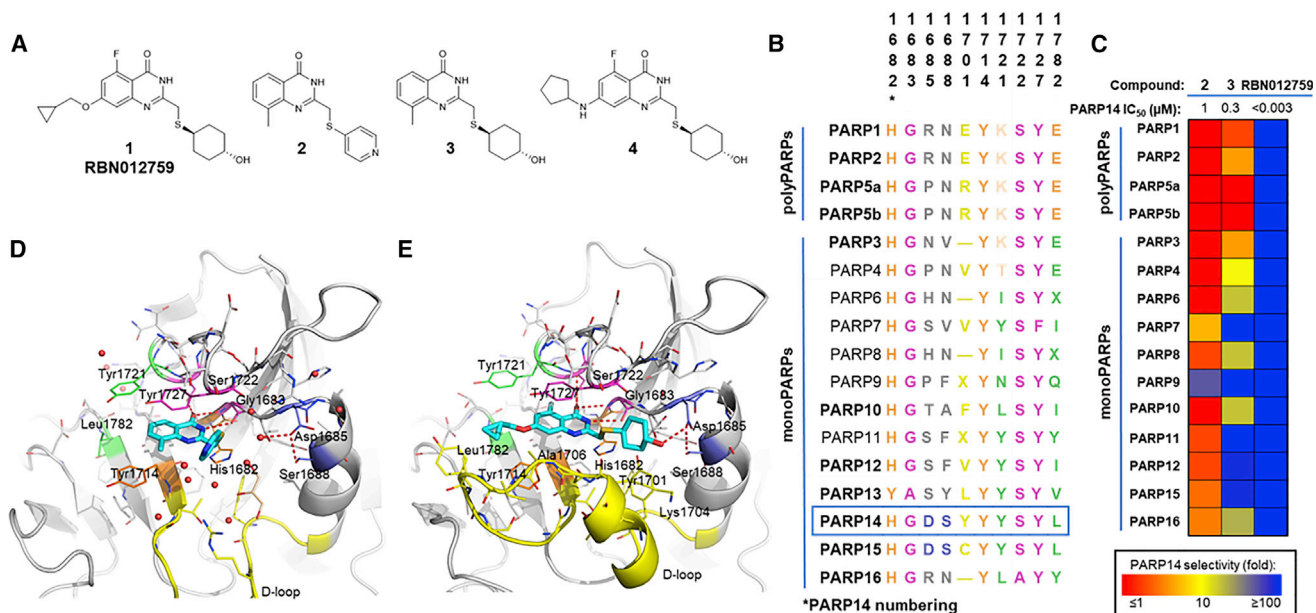


Figure 1. Structure-based optimization and PARP family selectivity of PARP14 inhibitors

(A) Structures of compounds 1–4.

(B) PARPs structure and sequence alignments for key residues in the active site. The numbering of amino acid residues is in reference to PARP14 residue numbering. PARPs that have been characterized by X-ray crystallography are highlighted in bold letters and were aligned based on their three-dimensional structures. PARPs that have not been structurally characterized were aligned based on sequence. Residues that could not be predicted by sequence alignment are represented as an X. Canonical HYE motifs for PARP-polyenzymes are colored orange. For PARP-monoenzymes, the residue that overlaps with the canonical E residue is colored in green (Leu1782 for PARP14) and comprises part of the MAR/PAR pair of residues (1782/1721). Conserved residues that contribute to binding of most PARP ligands are colored in magenta. The residue in the PARP14 D loop that contributes to selectivity (Y1701) is in yellow and the Asp/Ser pair (1685/1688) targeted for PARP14 selectivity is in purple.

(C) PARP14 TR-FRET IC₅₀ values, represented as geometric means ± SD, and PARP family selectivity of compounds 2, 3, and RBN012759, represented as fold selectivity for PARP14.

(D and E) Cartoon diagrams of PARP14 crystal structures with ligands drawn as cyan sticks, compound 2 (D) and RBN012759 (E). Hydrogen bonds are drawn as red dashes. Residues are colored as described in (C)

Schweiker et al., 2018). Limited PARP family selectivity data for previous PARP14 inhibitors has been disclosed and, when measured, the selectivity for PARP14 over the PARP-monoenzymes in particular is typically less than 10-fold. We sought to identify a highly potent and selective inhibitor of PARP14 to enable exploration of PARP14-mediated biology. Here, we describe the discovery and characterization of an *in vitro* and *in vivo* chemical probe, RBN012759 (1), which inhibits PARP14 catalytic activity with an IC₅₀ of 0.003 μM and with >300-fold selectivity over all PARP family members. Catalytic inhibition of PARP14 with RBN012759 leads to repolarization of M2-like macrophages to a less immunosuppressive phenotype and induction of inflammation markers in kidney cancer explants.

RESULTS

Structure-based optimization to identify RBN012759

Screening a PARP-preferring compound collection with a previously described PARP14 self-modification DELFIA assay (Wigle et al., 2019) identified compound 2 (Figure 1A), a close structural analog of a known pan-PARP inhibitor (Wahlberg et al., 2012), with an IC₅₀ of 1 μM. An X-ray co-crystal structure of 2 bound to PARP14 confirmed that it binds in the NAD⁺ pocket and makes several interactions, including hydrogen bonds between

the quinazolinone NH and Gly1683 backbone carbonyl, the quinazolinone carbonyl and Ser1722 side-chain OH, and a pi-stacking interaction with Tyr1727 (Figure 1D). The thiopyridine moiety, which is positioned in an area of the pocket lined on one side by the flexible D loop (Wahlberg et al., 2012), does not make interactions with the protein and the D loop is disordered.

Despite having relatively weak PARP14 potency and poor PARP family selectivity (Figure 1C; Table S2), 2 provided a hit that enabled modular synthesis of analogs to probe PARP14 potency and selectivity structure-activity relationships (SAR). Compound 2 also presented vectors that were well suited to pursue structure-based hypotheses for improving potency and selectivity in two key regions of the binding pocket. The thiopyridine moiety of 2 is near an area of the pocket formed on one side by Ser1688 and Asp1685, residues that are unique among the PARP family to only PARP14 and PARP15 (Figure 1B). Ser1688 and Asp1685 engage each other via a hydrogen bond and interact with a water molecule, an interaction that we hypothesized could be displaced by an inhibitor. Optimization of the thiopyridine portion of 2 included derivatives designed to engage the Asp1685/Ser1688 motif and add a favorable interaction to improve potency and selectivity. Diverse thioether substituents were synthesized while holding the methylquinazolinone constant. PARP14 potency for all analogs was determined using a

PARP14 probe displacement assay with time-resolved fluorescence energy transfer (TR-FRET) readout (Wigle et al., 2020), and to build selectivity SAR, analogs were screened in a complete panel of PARP family biochemical assays (Wigle et al., 2019). The *trans*-cyclohexanol-containing compound **3** was prepared (Figure 1A), and it provided a 3-fold improvement in PARP14 potency ($IC_{50} = 0.3 \mu M$) versus **2** with a significant improvement in selectivity over all PARP-monoenzymes (Figure 1C; Table S2).

A second region of the PARP14 binding pocket targeted to gain selectivity over the PARP-polyenzymes, referred to as the MAR/PAR difference region, due to key residue differences between the PARP-polyenzymes and PARP-monoenzymes, is located at a site defined by Tyr1721 and Leu1782. While the PARP-polyenzymes contain a salt bridge formed by Lys and Glu residues (Vyas et al., 2014), where the Glu is part of the conserved HYE motif, most PARP-monoenzymes contain hydrophobic residues at these positions (Figure 1B). Seeking to exploit this polarity difference between the PARP-monoenzymes and -polyenzymes, we incorporated hydrophobic moieties into the quinazolinone core that would project into the MAR/PAR difference region. Keeping the *trans*-cyclohexanol moiety of **3** in place, it was determined that substitution off the 7-position of the quinazolinone core improved potency. Optimization led to incorporation of a 7-cyclopropylmethanol substituent and a fluorine atom at the 5-position of the quinazolinone, with no substitution at the 6- and 8-positions, to give compound **1** (RBN012759, Figure 1A). RBN012759 has an IC_{50} of $0.003 \mu M$ in the PARP14 TR-FRET probe displacement assay and has >300-fold selectivity over the other PARP-monoenzymes and >1,000-fold selectivity over the PARP-polyenzymes (Figure 1C; Table S1). Several previously reported PARP14 inhibitors were profiled in our PARP assay panel and were substantially less potent and selective PARP14 inhibitors than RBN012759 (Table S4).

An X-ray co-crystal structure of RBN012759 bound to PARP14 illustrates its binding mode (Figure 1E). RBN012759 binds to the PARP14 NAD^+ pocket and retains the hydrogen bonds and pi-stacking interaction observed with **2**. Relative to the thiopyridine moiety of **2**, the conformation of the thio-*trans*-cyclohexanol group of RBN012759 is shifted toward the Asp1685 and Ser1688 residues, and the alcohol of the cyclohexyl group interacts with Asp1685, displacing the water molecule observed in the structure of PARP14 bound to **2**. This conformational change of the thioether enables the D loop in the RBN012759 structure to adopt an ordered, "closed" conformation in which the *trans*-cyclohexanol also engages the D loop residues Tyr1701 and Lys1704 in van der Waals interactions. Overlay of the compound **2**/PARP14 and RBN012759/PARP14 X-ray co-crystal structures (Figure S1A) illustrates that a steric clash would occur between the thiopyridine of **2** in its binding conformation and the D loop in the closed conformation.

The co-crystal structure of RBN012759 with PARP14 also highlights determinants for the observed improvement in PARP-polyenzyme selectivity (Figure 1E). The 7-cyclopropylmethanol group makes several van der Waals interactions in the hydrophobic region lined by the MAR/PAR difference residues and part of the D loop, including residues Leu1782, Ala1706, and Tyr1714. Overlay of the compound **3** and

RBN012759 X-ray co-crystal structures (Figure S1B) illustrates that optimization in the MAR/PAR difference region had little effect on the thioether portion of the molecule, as the *trans*-cyclohexanol groups are well overlaid. Based on its superior PARP14 potency and PARP family selectivity, we characterized RBN012759 further to confirm its suitability as a chemical probe.

Biophysical and pharmacokinetic characterization of RBN012759

The PARP14 binding affinity of RBN012759 ($K_d = 0.002 \mu M$) was determined by surface plasmon resonance (SPR) using the immobilized catalytic domain of PARP14 (Figure 2A), which correlates well with the IC_{50} ($0.003 \mu M$) determined from the PARP14 TR-FRET probe displacement assay. RBN012759 retained at least this level of potency when measured in a full-length PARP14 enzymatic auto-modification assay in the DELFIA format, in which it returned an IC_{50} value that was below the limit of quantification of the assay ($<0.005 \mu M$). In a thermal shift assay, RBN012759 stabilized the human PARP14 catalytic domain by $11^\circ C$ (Figure 2B). RBN012759 inhibited a mouse PARP14 TR-FRET probe displacement assay with an IC_{50} value ($0.005 \mu M$) that is comparable with its human PARP14 potency, suggesting that RBN012759 is also a suitable chemical probe for evaluating the role of PARP14 in mouse systems. RBN012759 has solubility at pH 7.4 of $198 \mu M$, with good permeability and minimal efflux in MDR1 overexpressing MDCK cells ($P_{app,A-B} = 15 \times 10^{-6} \text{ cm/s}$, efflux ratio = 2) and Caco-2 cells ($P_{app,A-B} = 19 \times 10^{-6} \text{ cm/s}$, efflux ratio = 1). After intravenous administration in CD-1 mice, RBN012759 had a clearance of 54 mL/min/kg with a half-life of 0.4 h and steady state volume of distribution of 1.4 L/kg . RBN012759 demonstrated oral bioavailability (30% F) at 100 mg/kg that decreased to 10% F at 500 mg/kg . Despite being modestly orally bioavailable, RBN012759 maintained exposure that provided 90-fold coverage of the mouse PARP14-free IC_{50} value (15 ng/mL) at 8 h following a 500 mg/kg oral dose.

Cellular PARP14 target engagement with RBN012759

The ability of RBN012759 to inhibit intracellular PARP14 was confirmed via orthogonal methods. A PARP14 NanoBRET probe displacement assay was developed in 293T cells that measures inhibition of bioluminescence resonance energy transfer (BRET) between NanoLuc-tagged PARP14 and an active site probe containing a fluorescent group. RBN012759 exhibited concentration-dependent inhibition of the BRET signal with an IC_{50} value of $0.003 \mu M$ (Figure 2C). When tested across a panel of PARP-monoenzyme NanoBRET assays (PARP7, PARP10, PARP11, PARP12, and PARP16), RBN012759 showed similar levels of potency as that observed in enzyme assays (Table S1), suggesting that it is also highly selective in cells.

Since PARP14 is a known ISG, assays were developed in IFN- γ -stimulated mouse RAW264.7 cells and primary human macrophages to demonstrate target engagement on endogenous PARP14. Treatment with RBN012759 led to a concentration-dependent increase in PARP14 protein, a phenomenon that was described previously in other models (Yoneyama-Hirozane et al., 2017; Scaltriti et al., 2009), with half-maximal effective concentration values of $0.01 \mu M$ in RAW264.7 cells and $0.08 \mu M$ in human macrophages (Figures 2D and 2E).

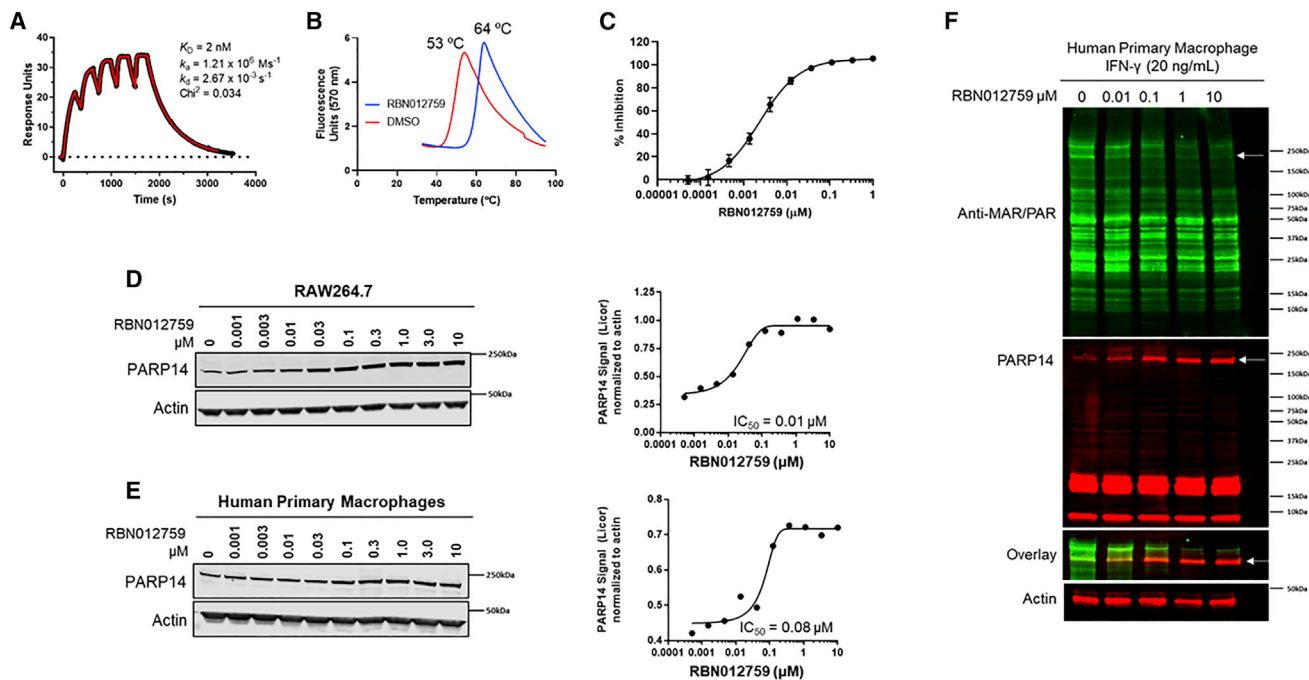


Figure 2. Biophysical characterization and intracellular engagement of PARP14 with RBN012759

(A) PARP14 SPR assay data. PARP14 catalytic domain having an N-terminal biotin-Avi tag was immobilized on a streptavidin-coated sensor chip and RBN012759 binding was analyzed using single-cycle kinetics.
 (B) PARP14 thermal shift assay data. The red curve represents PARP14 melting in the presence of 3% DMSO, and the blue curve represents PARP14 melting in the presence of 167 μM RBN012759. Data are representative of two independent experiments.
 (C) Ten-point IC_{50} curve for RBN012759 in the PARP14 NanoBRET biophysical cellular assay. The NanoBRET half-maximal effective concentration (EC_{50}) is $0.003 \mu\text{M} \pm \text{SD } 0.0009 \mu\text{M}$ from six independent experiments.
 (D) Western blot and IC_{50} curve with treatment of RAW264.7 cells with varying concentrations of RBN012759 following stimulation with 20 ng/mL IFN- γ .
 (E) Western blot and EC_{50} curve with treatment of primary human macrophages with varying concentrations of RBN012759 following stimulation with 20 ng/mL IFN- γ .
 (F) PARP14 and MAR/PAR protein expression by western blot analysis of human primary macrophages stimulated with 20 ng/mL IFN- γ and treated with increasing concentrations of RBN012759 for 48 h.

We next evaluated the ability of RBN012759 to inhibit PARP14-specific self-MARylation. MARylation was detected by immunoblot using an antibody that binds to both MAR and PAR (Lu et al., 2019) and a PARP14 antibody in IFN- γ -stimulated primary human macrophages (Figure 2F). RBN012759 decreased the MAR/PAR signal corresponding to PARP14-self-MARylation in a concentration-dependent manner, further supporting its activity on endogenous PARP14 (Figure 2F). A minor MAR/PAR signal remained after treatment, suggesting that PARP14 may be a substrate of additional PARP enzymes (Figure 2F). To reinforce the specificity of PARP14 autoMARylation, we used the CFPAC-1 cell line due to its high endogenous PARP14 baseline level and response to IFN- γ stimulation by increasing PARP14 and ADP-ribosylation. First, endogenous PARP14 was immunoprecipitated from IFN- γ -stimulated CFPAC-1 cells and probed for MAR/PAR (Figure S2C). These data demonstrated that PARP14 auto-MARylation is stimulated by IFN- γ and robustly inhibited by RBN012759 (Figure S2C). In addition, CFPAC-1 cells were stimulated with IFN- γ to increase PARP14 expression and MARylation and treated with increasing concentrations of RBN012759 (Figure S2D). RBN012759 decreased the MARylation signal in a concentration-dependent manner, similar to that observed in human macrophages (see

Figure S2D). The same effect was not observed with niraparib treatment, a PARP1 inhibitor, in IFN- γ -stimulated CFPAC-1 cells (Figure S2E). The major effect of RBN012759 was observed under IFN- γ -stimulated conditions rather than unstimulated baseline conditions (Figures S2E and S2D). Altogether these data show that the reduced MARylation signal after RBN012759 treatment corresponds to PARP14 self-MARylation.

To further demonstrate target engagement, compound 4 (Figure 1A), a PARP14 catalytic inhibitor that is a structural analog of RBN012759 with a similar potency and selectivity profile (Table S2), was used in a substrate identification experiment with IFN- γ -stimulated primary human macrophages. Proteins identified in the vehicle-treated samples and reduced in the PARP14 inhibitor-treated samples were considered as potential PARP14 substrates (Figure 3A). A subset of interferon-related proteins, including OAS2, STAT2, STAT1, and MX1, showed reduced spectral counts in the PARP14 inhibitor-treated samples, suggesting that these proteins may be potential substrates of PARP14 (Figure 3B; Table S5). Our data identified previously reported PARP14 putative substrates, such as STAT1, pointing to its role in macrophage polarization and immune responses (Iwata et al., 2016; Caprara et al., 2018; Carter-O'connell et al., 2018).

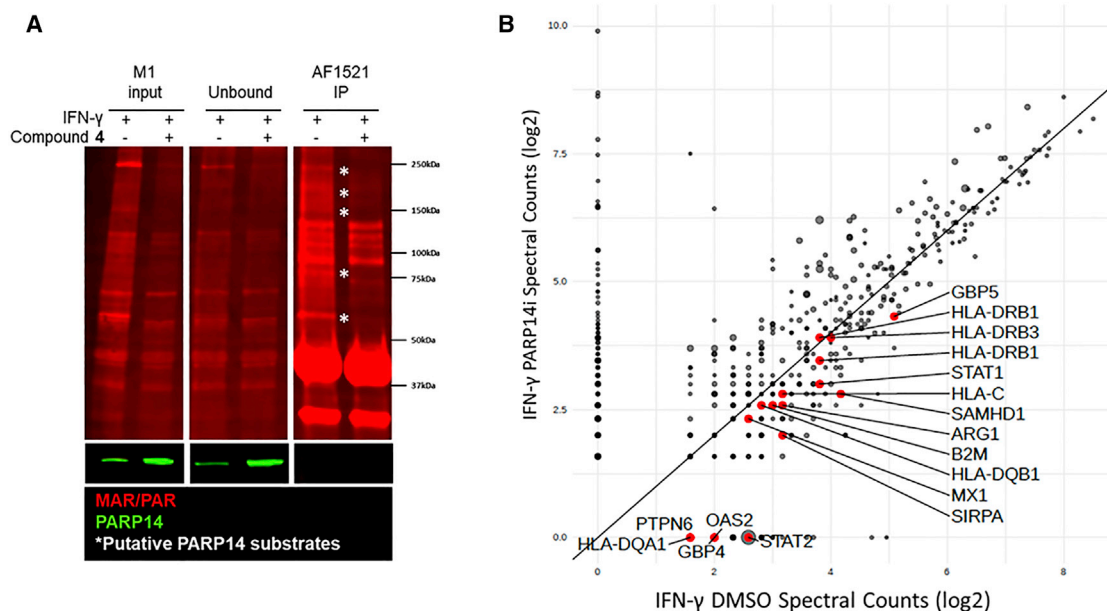


Figure 3. Compound 4 is active in cells and inhibits MARYlation of inflammation-related proteins

(A) MAR/PAR and PARP14 protein expression signals were determined by immunoblot analysis in human primary macrophages prepared as described in Figure 2E and treated with 10 μ M of compound 4. Protein lysate pre- and post-immunoprecipitation with Af1521-conjugated magnetic resin was analyzed by immunoblot and putative PARP14 substrates are marked by the white asterisks (*).

(B) Scatterplot of log-transformed spectral counts from PARP14 substrate identification screen in primary human macrophages. Interferon GeneSet genes enriched in both substrate and transcriptional experiments upon PARP14 inhibitor treatment are highlighted in red.

In vivo target engagement with RBN012759

The ability of RBN012759 to engage PARP14 *in vivo* was also evaluated. C57BL/6 mice were treated with RBN012759 at 300 and 500 mg/kg BID PO for 7 days, during which it was well tolerated with no significant body weight loss observed. The mice were sacrificed at 12 h following the final dose, and spleen, a tissue with endogenous PARP14 expression (Cho et al., 2009), was collected for determination of PARP14 protein levels. As observed with treatment of cells *in vitro* (see Figure 2D), treatment with RBN012759 led to an increase in PARP14 protein *in vivo*. The 500 mg/kg treatment group showed increased PARP14 protein, while the 300 mg/kg group did not, correlating with RBN012759 plasma exposures at the 12 h time point in which the mouse PARP14-free IC₅₀ value was increased by 6- and <1-fold, respectively (Figures S2F–S2H). These data support the use of RBN012759 as an *in vivo* chemical probe that selectively engages PARP14 in tissue.

Catalytic inhibition of PARP14 reverses IL-4-driven gene expression in M2-like macrophages

With a suitable chemical probe in hand, we next investigated whether PARP14 catalytic inhibition phenocopies the published effects of PARP14 knockout on IFN- γ (M1-like)- and IL-4 (M2-like)-driven macrophage polarization. Treatment of primary human macrophages with IFN- γ elicited typical interferon response gene expression changes (Figure S3A). RBN012759 co-treatment for 6 and 24 h did not change IFN- γ -driven gene expression dramatically (Figure S3B). This contrasts with data published in mouse macrophages, where genetic PARP14 KO exacerbates the IFN- γ response and suggests that the effects on the

M1-like polarization may involve domains other than the catalytic domain of PARP14 (Iwata et al., 2016).

IL-4-stimulated human primary macrophages were used to investigate if catalytic inhibition of PARP14 decreased protumor M2-like macrophage polarization, as suggested by the published PARP14 KO data in mouse macrophages (Iwata et al., 2016) (Figure 4A). Gene expression changes of IL-4-polarized M2-like macrophages treated with RBN012759 clustered with naive-M0 macrophage signatures (Figure 4B), suggesting that PARP14 inhibition reversed the IL-4-driven skewing closer to the naive M0 phenotype. Unsupervised clustering analysis uncovered five distinct clusters of differentially expressed genes that distinguished IL-4 vehicle (M2-like) versus RBN012759-treated macrophages (Figure 4C; Table S6). Cluster 4 revealed significantly increased genes, including *CD209* in RBN012759-treated M2-like macrophages. *CD209* is a pathogen-recognition receptor that mediates the endocytosis function of macrophages (Schulz et al., 2019). Several markers typically expressed by inflammatory actively phagocytic macrophages, *MMP-1* (cluster 4) and *CLTC* (cluster 1) (Huang et al., 2012; Steenport et al., 2009; Gong et al., 2008; Liu et al., 2014), were also upregulated with RBN012759. Cluster 3 revealed a group of downregulated mitochondria metabolism-related genes, such as *ATP5D*, *ETFB*, and *VDAC2*. These data align with studies suggesting that inflammatory macrophages increase glycolytic activity while decreasing oxidative phosphorylation of mitochondria (Jung et al., 2018; Viola et al., 2019). Cluster 5 revealed upregulation of a key inflammatory chemokine, *CCL13*, which attracts monocytes, lymphocytes, basophils, and eosinophils to inflammatory sites.

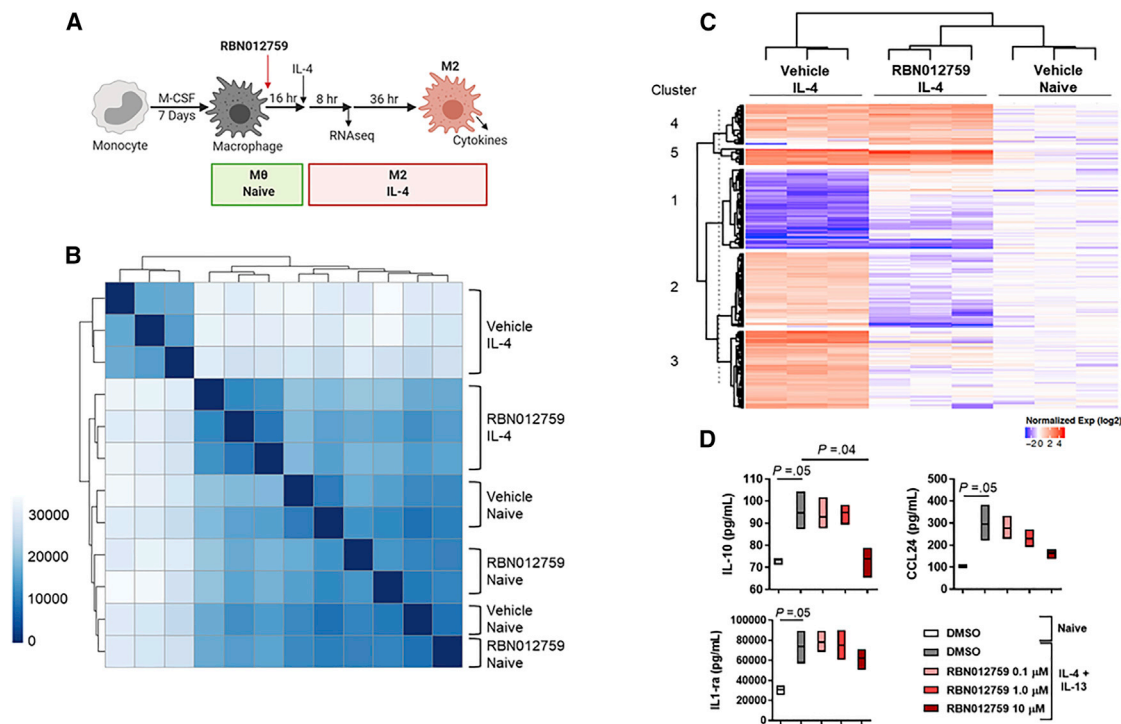


Figure 4. Inhibition of PARP14 with RBN012759 dampens the M2-like macrophage protumor phenotype

(A) M2-like polarization of primary human macrophages with IL-4 (15 ng/mL; M2-like) and treatment with RBN012759 to determine impact on gene expression. (B) Heatmap and hierarchical clusters representing the transcriptional distances between vehicle and RBN012759-treated samples based on a Poisson distance metric. (C) Heatmap and hierarchical clusters using normalized gene expression values from differentially expressed genes with IL-4 + vehicle or RBN012759 + IL-4 treatments. (D) Levels of IL-10, CCL24, and IL-1ra in naive M0 or M2-like (IL-4 + IL-13) macrophage culture supernatants (three biological replicates) were determined 48 h after treatment with RBN012759. Statistical significance we determined by Welch's t-test.

RBN012759 treatment also decreased the protein level of three M2-like proteins, IL-10, CCL24, and IL1-ra, in the supernatants of IL-4-stimulated macrophages to a level closer to baseline (i.e., not stimulated with IL-4, Figure 4D). IL-10 is an IL-4-elicited anti-inflammatory protumor cytokine that is secreted by various immune cell types in the tumor microenvironment (TME), including tumor-associated macrophages (Cheng et al., 2019). CCL24 and IL1-ra are also associated with the M2-like phenotype (Shapouri-Moghaddam et al., 2018; Pechkovsky et al., 2010; Makita et al., 2015). As expected, IL-4 alone or in combination with IL-13 increased STAT6 phosphorylation in M2-like macrophages; however, no changes in phospho-STAT6 were observed with RBN012759 treatment at the evaluated time point (Figure S3F). This is in contrast with a previously reported negative effect on STAT6 phosphorylation with PARP14 genetic depletion and points to a potential difference between catalytic inhibition and complete protein depletion (Iwata et al., 2016).

Apart from a minor subset of genes, RBN012759 treatment mostly led to negative changes in gene expression in the M2-like macrophage model system (Figures 4C, S4C, and S4D). RBN012759 effects were observed across genes with both high and low expression levels (Figure S3E). The finding that PARP14 catalytic inhibition reverses IL-4-driven gene expression in macrophages suggests a role of PARP14 as a positive

regulator of the M2-like protumor phenotype. These data suggest that catalytic inhibition of PARP14 with RBN012759 changes M2-like macrophages toward a less immunosuppressive phenotype.

RBN012759 promotes inflammatory gene expression in human kidney cancer tumor explants

The observation that treatment with RBN012759 led to a decreased M2-like immunosuppressive macrophage phenotype prompted us to explore a model system that includes a complete tumor immune infiltrate and may more closely resemble the human tumor setting. To do so, *PARP14* gene expression was evaluated in a variety of tumors in The Cancer Genome Atlas (TCGA) and found to be significantly overexpressed in kidney renal clear cell carcinoma (KIRC) as compared with normal kidney tissue (Figure S4A). Moreover, analysis of TCGA KIRC patient data revealed an association between high *PARP14* gene expression and a significantly lower probability of survival (Figure S4B). Tumor *PARP14* expression positively associated with signatures of various immune cells, including macrophages, and negatively associated with tumor purity, as assessed by the Tumor Immune Estimation Resource (Li et al., 2016) (Figure S4C). This suggests that the increased *PARP14* expression in kidney cancer is at least in part due to increased expression in the tumor immune infiltrate. For these reasons, we investigated the effects of

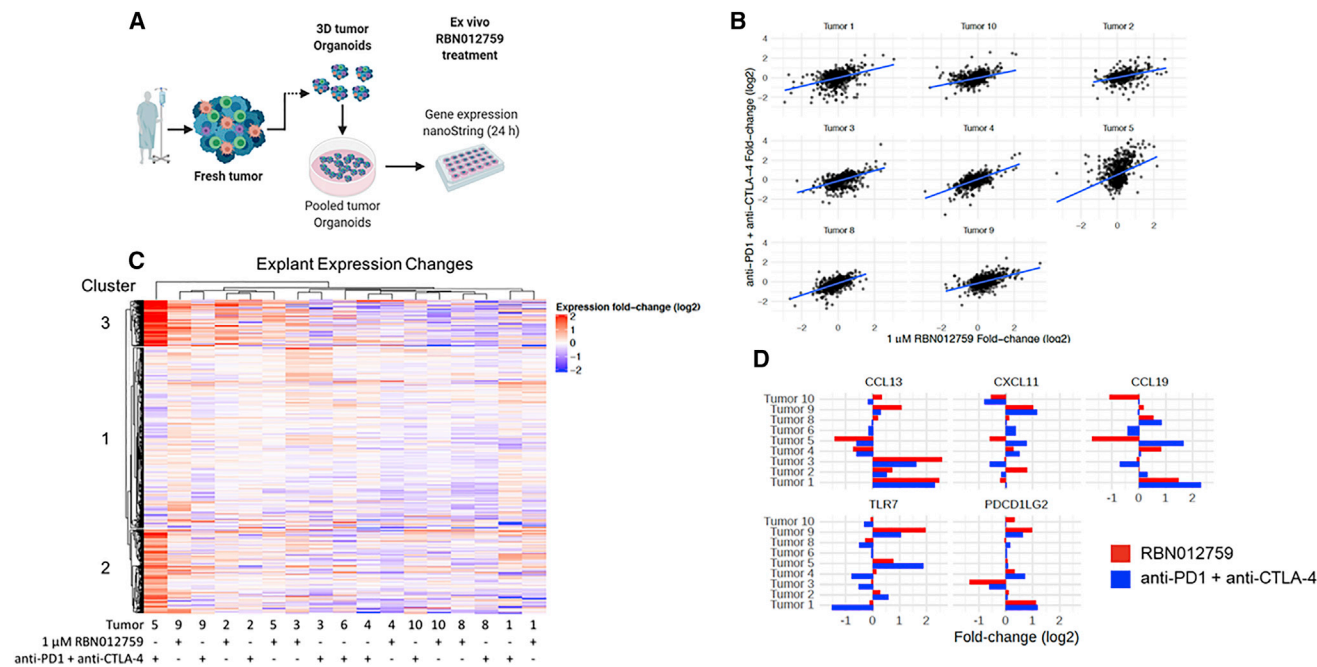


Figure 5. RBN012759 induces antitumor inflammation in kidney cancer tumor explant models

(A) Cartoon depiction of renal clear cell carcinoma tumor explant culture assay.

(B) Biplots of the treatment-based gene expression changes comparing PARP14 inhibitor treatment (1 μ M RBN012759) and anti-PD-1 (3 μ g/mL) + anti-CTLA-4 (3 μ g/mL) treatment for the ten bulk explant tumor samples.

(C) Heatmap and hierarchical clusters showing expression changes in ten bulk explant tumor samples from PARP14 inhibitor treatment (1 μ M RBN012759) or anti-PD-1 (3 μ g/mL) + anti-CTLA-4 (3 μ g/mL) treatment.

(D) Barplots indicating the treatment-based expression fold changes for select genes from PARP14 inhibitor treatment with RBN012759 (red) and anti-PD-1 + anti-CTLA-4 treatment (blue) for the 10 bulk explant tumor samples.

RBN012759 on KIRC human tumor explants (Page et al., 2018; Mediavilla-Varela et al., 2018). Ten KIRC tumors were treated with RBN012759, vehicle, or the combination of anti-PD-1 and anti-CTLA-4 (immune checkpoint inhibitor [ICI]), and RNA was isolated 24 h after treatment initiation for gene expression analysis (Figures 5A and S4D). A positive correlation of gene expression changes between ICI and RBN012759 treatments was observed across all tumors tested (Figure 5B), but neither RBN012759- nor ICI-induced expression changes correlated with those elicited by co-treatment with phorbol-12-myristate-13-acetate and ionomycin, a general inflammatory stimulus (Figure S4E). Unsupervised clustering analysis of gene expression data revealed that a subset of RBN012759-treated tumors clustered with ICI-sensitive tumors (Figure 5C). Among the genes significantly modulated with RBN012759 were several chemokines associated with antitumor inflammation, including CXCL11, CCL19, and CCL13 (Figure 5D). Toll-like receptor 7 (TLR7), a key component of innate and adaptive immunity, was also upregulated with RBN012759 or ICI treatment in tumors 5 and 9 (Figure 5D). The immune checkpoint ligand PD-L2, a known marker of T cell activation, was upregulated in tumors 1 and 9 upon treatment with either RBN012759 or ICI (Figure 5D). The variability in RBN012759-driven gene expression changes that correlate to response to ICI treatment is not entirely unexpected, since KIRC tumors are characterized by highly variable tumor infiltrating lymphocytes (TILs) and macrophage infiltration and are known to have response rates ranging from 20% up to

60% (Santoni et al., 2018; Motzer et al., 2018). Altogether, these data revealed that PARP14 inhibition with RBN012759 elicited similar gene expression changes as ICI combination therapy, an approved treatment for kidney cancer, in subsets of kidney cancer tumor explants (Motzer et al., 2018).

DISCUSSION

Here, we describe the development of RBN012759, a chemical probe that inhibits PARP14 with an IC_{50} value of 0.003 μ M and has high selectivity over all PARP family enzymes. Medicinal chemistry efforts that began with an unselective, micromolar screening hit were enabled by a detailed understanding of PARP family NAD^+ binding pockets. Hit 2 provided a template for targeting interactions in two key regions of the PARP14 NAD^+ binding pocket. The Ser1688/Asp1685 motif, which is unique to PARP14 and PARP15, was targeted to improve PARP14 potency and selectivity over the other PARP-monoenzymes. The MAR/PAR difference region, which contains a conserved HYE motif in which the Glu forms a salt bridge in the PARP-polyenzymes but contains HY(I/L/Y) in the PARP-monoenzymes, was targeted with hydrophobic substituents. It was anticipated that this strategy would disfavor interactions with the PARP-polyenzymes, and indeed a series of PARP11 inhibitors for which selectivity over the PARP-polyenzymes was obtained in a similar manner has been described (Kirby et al., 2018).

Optimization of the thiopyridine moiety in compound **2** to target displacement of the water atom bound to Ser1688/Asp1685 led to **3**, which incorporates a *trans*-cyclohexanol moiety that was maintained in RBN012759. X-ray co-crystal structures of **3** and RBN012759 with PARP14 show an interaction between the alcohol and Asp1685. The change of conformation of the thioether in going from the pyridine of **2** to the *trans*-cyclohexanol also enabled the PARP14 D loop to adopt an ordered, closed conformation, which may be preferred, as both **3** and RBN012759 engage the D loop in favorable van der Waals interactions. The interaction with Tyr1701 may contribute to the observed selectivity over PARP15, which has a Cys residue at this position (Figure 1B). Optimization of the portion of the inhibitors that binds in the Asp/Ser region of the pocket enabled interactions with the protein that both increased PARP14 potency and decreased potency against the other PARP-monoenzymes.

Efforts to project hydrophobic groups into the MAR/PAR difference region led to incorporation of a cyclopropylmethyl ether at the 7-position of the quinazolinone, which gave significant improvements in selectivity favoring PARP14 over the PARP-polyenzymes coupled with additional improvement in PARP14 potency. Since the thioether moieties of **2** and RBN012759 adopt the same conformation in the binding pocket (Figure S1B), improvements in potency and selectivity are attributed to interactions in the MAR/PAR difference region. RBN012759 is >300-fold selective over all PARP-monoenzymes and demonstrates similarly high selectivity over the PARP-polyenzymes (>1,000-fold), a substantial improvement over previously reported inhibitors (Table S4).

Additional characterization of RBN012759 demonstrated its utility as both an *in vitro* and *in vivo* chemical probe. RBN012759 has sufficient solubility at pH 7.4, is highly permeable, and is not likely a substrate of Pgp or BCRP. Multiple orthogonal methods were used to demonstrate that RBN012759 inhibits PARP14 intracellularly. Its potency in the PARP14 NanoBRET probe displacement assay correlated well with both enzymatic assay data and binding affinity generated by SPR, and the selectivity for PARP14 observed in enzyme assays was reproduced in a panel of PARP-monoenzyme biophysical cellular assays. Robust, concentration-dependent stabilization of PARP14 and inhibition of MARYlation were observed in IFN- γ -stimulated primary human macrophages, confirming that RBN012759 inhibits endogenous PARP14. Dose-dependent stabilization of PARP14 was also observed in mouse spleen tissue. With a pharmacokinetic profile enabling continuous target coverage with oral, twice-daily dosing, RBN012759 can be utilized to evaluate the effects of PARP14 in the *in vivo* setting. RBN012759 provides the ability to evaluate the effects of PARP14 catalytic inhibition with a potent, selective chemical probe in both *in vitro* and *in vivo* settings.

Clinical and experimental studies have demonstrated that macrophages are amply present in the TME of most tumor types and have a key regulatory role in tumor progression (Noy and Pollard, 2014). Given the general abundance of macrophages in most cancers, repolarization of macrophages toward an inflammatory function may prove efficacious for multiple oncology indications. Our studies demonstrated that catalytic inhibition of PARP14 with RBN012759 led to decreased IL-4-driven M2-like gene expression in macrophages, suggesting that PARP14

inhibition results in a less immunosuppressive phenotype. Of note, catalytic inhibition of PARP14 in human macrophages did not entirely phenocopy the positive stimulatory effect of PARP14 KO on IFN- γ -driven gene expression observed in mouse macrophages (Iwata et al., 2016), at least under the conditions and time points tested in our studies. This points to a possible non-catalytic function of PARP14 in the IFN- γ pathway in normal macrophages. However, RBN012759 increased markers associated with active phagocytosis, such as *CD209*, *MMP-1*, and *CLTC*, in addition to reversing IL-4-driven gene expression. This suggests that PARP14 inhibition has the potential to increase the antitumor activity of macrophages in the tumor microenvironment. Although cancer immunotherapy currently benefits a significant fraction of cancer patients, many have primary or develop secondary (immunotherapy induced) resistance, which has been, in part, attributed to the presence of macrophages in the tumor microenvironment (Pathria et al., 2019). Targeting tumor-associated macrophages has been proposed as a viable therapeutic strategy to reverse immunosuppression. Repolarization of tumor-associated macrophages is one of the most promising strategies currently being explored and targeting PARP14 may be a viable strategy for this therapeutic hypothesis.

The immunosuppressive role of PARP14 was evaluated in human tumor explants to recapitulate the human tumor setting, where PARP14 is overexpressed, more closely than in cellular or mouse systems. Catalytic inhibition of PARP14 with RBN012759 in KIRC human tumor explants revealed significant increases in several pro-inflammatory chemokines, including CCL13, which was also upregulated in cultured normal macrophages after PARP14 inhibition. *TLR7*, also upregulated with RBN012759 treatment, is being explored as a target to achieve macrophage repolarization via agonist molecules that stimulate the innate immune response (Pathria et al., 2019). Intriguingly, PARP14 inhibition elicited similar gene expression changes in tumor explants as ICI combination therapy, an active regimen in kidney cancer (Motzer et al., 2018). This suggests potential utility of PARP14 inhibitors in this cancer type as single agent and/or in combination with ICI therapy.

The discovery of RBN012759, a potent and highly selective *in vitro* and *in vivo* chemical probe of PARP14, enabled the efforts described here to link PARP14 with suppression of the antitumor immune response. It is our hope that RBN012759 will serve as a useful tool for further exploration of PARP14 functions in cell biology and as a drug target.

SIGNIFICANCE

PARP14 is an interferon-stimulated gene (ISG) that is overexpressed in tumors compared with normal tissues and has been implicated by genetic knockout studies to promote protumor macrophage polarization and suppress the antitumor inflammatory response due to its role in modulating IL-4 and IFN- γ signaling pathways. Efforts to further explore and validate the role of PARP14 have been hampered by a lack of potent, highly selective PARP14 inhibitors. Here, we describe the discovery of a chemical probe, RBN012759, whose profile represents a substantial improvement over previously reported tool compounds. RBN012759 inhibits PARP14 with an IC₅₀ of 0.003 μ M, exhibits >300-fold selectivity over all

mono- and PARP-polyenzyme family members, and is a cell-permeable, soluble probe that achieves continuous target coverage in mice with oral dosing. RBN012759 inhibits MARylation in primary human macrophages and demonstrates robust stabilization of endogenous PARP14 in cells and *in vivo*. Inhibition of PARP14 with RBN012759 reverses IL-4-driven protumor gene expression in macrophages and induces an inflammatory mRNA signature similar to immune checkpoint inhibitor therapy in primary human tumor explants. These data support an immune suppressive role of PARP14 in tumors and suggest potential utility of PARP14 inhibitors in the treatment of cancer.

STAR★METHODS

Detailed methods are provided in the online version of this paper and include the following:

- KEY RESOURCES TABLE
- RESOURCE AVAILABILITY
 - Lead contact
 - Materials availability
 - Data code and availability
- EXPERIMENTAL MODEL
 - Cell lines
 - *In vivo* animal studies
- METHOD DETAILS
 - Assay and chemistry reagents
 - Chemistry
 - Protein purification and crystallography
 - Human PARP14 catalytic domain *in vitro* active site probe displacement (TR-FRET) assay
 - Human full-length PARP14 self-modification enzymatic activity (DELFI) assay
 - Mouse catalytic domain PARP14 *in vitro* active site probe displacement (TR-FRET) assay
 - PARP14 SPR assay
 - Human PARP14 catalytic domain thermal shift assay (TSA)
 - PARP14 NanoBRET cellular biophysical assay
 - Human primary macrophage culture
 - Cytokine and chemokine measurements
 - Immunoblotting
 - NanoString Assay and analysis
 - RNA sequencing and analysis
 - Substrate identification
 - Human tumor explant culture and RNA extraction
 - TCGA analysis
 - *In vivo* pharmacokinetics and bioanalysis
 - *In vivo* target engagement
- QUANTIFICATION AND STATISTICAL ANALYSIS
 - % Inhibition
 - IC₅₀ curve fitting
 - Pass/fail criteria for screening plates

SUPPLEMENTAL INFORMATION

Supplemental information can be found online at <https://doi.org/10.1016/j.chembiol.2021.02.010>.

ACKNOWLEDGMENTS

We thank Jennifer Downing for collecting analytical data for all compounds, Andrew Santospago for compound handling and plating, Jeff Song for management of the tumor explant study, and Mark Boothby and James Audia for strategic input.

AUTHOR CONTRIBUTIONS

L.B.S., J.R.M., and K.K.S. prepared the manuscript with input from all authors. L.B.S. designed the compounds, supervised the chemistry team, and guided medicinal chemistry strategy. J.R.M. conceived, conducted, and oversaw biology experiments and guided biology strategy. K.K.S. oversaw X-ray crystallography and guided strategy. R.A. conducted computational biology analyses. D.J.B. and Y.R. developed and performed the NanoBRET assays. T.J.W. and W.D.C. developed and performed the PARP14 enzyme and thermal shift assays. T.J.W., W.D.C., and C.R.M. developed, performed, and oversaw the PARP family selectivity assays. T.J.W. oversaw the SPR assay. K.K. oversaw the *in vivo* target engagement study. K.G.K.-B. oversaw the KIRC explant study. A.Z.L. conducted substrate identification experiments with guidance from M.N. A.E.C. conducted the macrophage gene expression experiment. E.M. conducted the self-MARylation expression analysis. J.-R.M. and C.R. conducted cell assays. M.M.V., V.M.R., H.K., and K.W.K. guided strategy and supervised the work.

DECLARATION OF INTERESTS

L.B.S., K.K.S., M.M.V., and K.W.K. are co-inventors on pending patent application WO 2019/126443 and issued U.S. Pat. No. 10,562,891, both of which relate to quinazolinone inhibitors of PARP14 for the treatment of cancer and other diseases and are assigned to Ribon Therapeutics, Inc., of Cambridge, MA, USA.

Received: June 26, 2020

Revised: December 18, 2020

Accepted: February 11, 2021

Published: March 10, 2021

REFERENCES

- Aguiar, R.C., Takeyama, K., He, C., Kreinbrink, K., and Shipp, M.A. (2005). B-Aggressive lymphoma family proteins have unique domains that modulate transcription and exhibit poly(ADP-ribose) polymerase activity. *J. Biol. Chem.* **280**, 33756–33765.
- Aguiar, R.C.T., Yakushijin, Y., Kharbanda, S., Salgia, R., Fletcher, J.A., and Shipp, M.A. (2000). BAL is a novel risk-related gene in diffuse large B-cell lymphomas that enhances cellular migration. *Blood* **96**, 4328–4334.
- Andersson, C.D., Karlberg, T., Ekblad, T., Lindgren, A.E., Thorsell, A.G., Spjut, S., Uciechowska, U., Niemiec, M.S., Wittung-Stafshede, P., Weigelt, J., et al. (2012). Discovery of ligands for ADP-ribosyltransferases via docking-based virtual screening. *J. Med. Chem.* **55**, 7706–7718.
- Caprara, G., Prosperini, E., Piccolo, V., Sigismondo, G., Melacarne, A., Cuomo, A., Boothby, M., Rescigno, M., Bonaldi, T., and Natoli, G. (2018). PARP14 controls the nuclear accumulation of a subset of type I IFN-inducible proteins. *J. Immunol.* **200**, 2439–2454.
- Carter-O'connell, I., Vermehren-Schmaedick, A., Jin, H., Morgan, R.K., David, L.L., and Cohen, M.S. (2018). Combining chemical genetics with proximity-dependent labeling reveals cellular targets of poly(ADP-ribose) polymerase 14 (PARP14). *ACS Chem. Biol.* **13**, 2841–2848.
- Cheng, H., Wang, Z., Fu, L., and Xu, T. (2019). Macrophage polarization in the development and progression of ovarian cancers: an overview. *Front. Oncol.* **9**, 421.
- Cho, S.H., Goenka, S., Hentinen, T., Gudapati, P., Reinikainen, A., Eischen, C.M., Lahesmaa, R., and Boothby, M. (2009). PARP-14, a member of the B aggressive lymphoma family, transduces survival signals in primary B cells. *Blood* **113**, 2416–2425.

- Cho, S.H., Raybuck, A., Wei, M., Erickson, J., Nam, K.T., Cox, R.G., Trochtenberg, A., Thomas, J.W., Williams, J., and Boothby, M. (2013). B cell-intrinsic and -extrinsic regulation of antibody responses by PARP14, an intracellular (ADP-ribose)transferase. *J. Immunol.* *191*, 3169–3178.
- Cohen, M.S., and Chang, P. (2018). Insights into the biogenesis, function, and regulation of ADP-ribosylation. *Nat. Chem. Biol.* *14*, 236–243.
- Ekblad, T., Lindgren, A.E., Andersson, C.D., Caraballo, R., Thorsell, A.G., Karlberg, T., Spjut, S., Linusson, A., Schuler, H., and Elofsson, M. (2015). Towards small molecule inhibitors of mono-ADP-ribosyltransferases. *Eur. J. Med. Chem.* *95*, 546–551.
- Ekblad, T., Verheugd, P., Lindgren, A.E., Nyman, T., Elofsson, M., and Schuler, H. (2018). Identification of poly(ADP-ribose) polymerase macromodulator inhibitors using an AlphaScreen protocol. *SLAS Discov.* *23*, 353–362.
- Goenka, S., Cho, S.H., and Boothby, M. (2007). Collaborator of Stat6 (CoaSt6)-associated poly(ADP-ribose) polymerase activity modulates Stat6-dependent gene transcription. *J. Biol. Chem.* *282*, 18732–18739.
- Gong, Y., Hart, E., Shchurin, A., and Hoover-Plow, J. (2008). Inflammatory macrophage migration requires MMP-9 activation by plasminogen in mice. *J. Clin. Invest.* *118*, 3012–3024.
- Holeczek, J., Lease, R., Thorsell, A.G., Karlberg, T., Mccadden, C., Grant, R., Keen, A., Callahan, E., Schuler, H., and Ferraris, D. (2018). Design, synthesis and evaluation of potent and selective inhibitors of mono-(ADP-ribose)transferases PARP10 and PARP14. *Bioorg. Med. Chem. Lett.* *28*, 2050–2054.
- Huang, W.C., Sala-Newby, G.B., Susana, A., Johnson, J.L., and Newby, A.C. (2012). Classical macrophage activation up-regulates several matrix metalloproteinases through mitogen activated protein kinases and nuclear factor- κ B. *PLoS One* *7*, e42507.
- Iansante, V., Choy, P.M., Fung, S.W., Liu, Y., Chai, J.G., Dyson, J., Del Rio, A., D'santos, C., Williams, R., Chokshi, S., et al. (2015). PARP14 promotes the Warburg effect in hepatocellular carcinoma by inhibiting JNK1-dependent PKM2 phosphorylation and activation. *Nat. Commun.* *6*, 7882.
- Iwata, H., Goettsch, C., Sharma, A., Ricchiuto, P., Goh, W.W., Halu, A., Yamada, I., Yoshida, H., Hara, T., Wei, M., et al. (2016). PARP9 and PARP14 cross-regulate macrophage activation via STAT1 ADP-ribosylation. *Nat. Commun.* *7*, 12849.
- Jung, S.B., Choi, M.J., Ryu, D., Yi, H.S., Lee, S.E., Chang, J.Y., Chung, H.K., Kim, Y.K., Kang, S.G., Lee, J.H., et al. (2018). Reduced oxidative capacity in macrophages results in systemic insulin resistance. *Nat. Commun.* *9*, 1551.
- Juszczynski, P., Kutok, J.L., Li, C., Mitra, J., Aguiar, R.C., and Shipp, M.A. (2006). BAL1 and BBAP are regulated by a gamma interferon-responsive bidirectional promoter and are overexpressed in diffuse large B-cell lymphomas with a prominent inflammatory infiltrate. *Mol. Cell Biol.* *26*, 5348–5359.
- Kirby, I.T., Kojic, A., Arnold, M.R., Thorsell, A.G., Karlberg, T., Vermehren-Schmaedick, A., Sreenivasan, R., Schultz, C., Schuler, H., and Cohen, M.S. (2018). A potent and selective PARP11 inhibitor suggests coupling between cellular localization and catalytic activity. *Cell Chem. Biol.* *25*, 1547–1553 e12.
- Li, B., Severson, E., Pignon, J.C., Zhao, H., Li, T., Novak, J., Jiang, P., Shen, H., Aster, J.C., Rodig, S., et al. (2016). Comprehensive analyses of tumor immunity: implications for cancer immunotherapy. *Genome Biol.* *17*, 174.
- Liu, C., Wang, J., and Zhang, X. (2014). The involvement of MiR-1-clathrin pathway in the regulation of phagocytosis. *PLoS One* *9*, e98747.
- Lu, A.Z., Abo, R., Ren, Y., Gui, B., Mo, J.R., Blackwell, D., Wigle, T., Keilhack, H., and Niepel, M. (2019). Enabling drug discovery for the PARP protein family through the detection of mono-ADP-ribosylation. *Biochem. Pharmacol.* *167*, 97–106.
- Makita, N., Hizukuri, Y., Yamashiro, K., Murakawa, M., and Hayashi, Y. (2015). IL-10 enhances the phenotype of M2 macrophages induced by IL-4 and confers the ability to increase eosinophil migration. *Int. Immunol.* *27*, 131–141.
- Mediavilla-Varela, M., Page, M.M., Krehling, J., and Altiock, S. (2018). Characterization of the immune landscape and analysis of tumor response after anti-PD-1 blockade in a 3D ex vivo system of non-small lung cancer. *Cancer Res.* *78*.
- Mehrotra, P., Hollenbeck, A., Riley, J.P., Li, F., Patel, R.J., Akhtar, N., and Goenka, S. (2013). Poly(ADP-ribose) polymerase 14 and its enzyme activity regulates T(H)2 differentiation and allergic airway disease. *J. Allergy Clin. Immunol.* *131*, 521–531.e1–12.
- Mehrotra, P., Riley, J.P., Patel, R., Li, F., Voss, L., and Goenka, S. (2011). PARP-14 functions as a transcriptional switch for Stat6-dependent gene activation. *J. Biol. Chem.* *286*, 1767–1776.
- Motzer, R.J., Tannir, N.M., McDermott, D.F., Aren Frontera, O., Melichar, B., Choueiri, T.K., Plimack, E.R., Barthelemy, P., Porta, C., George, S., et al. (2018). Nivolumab plus ipilimumab versus sunitinib in advanced renal-cell carcinoma. *N. Engl. J. Med.* *378*, 1277–1290.
- Moustakim, M., Riedel, K., Schuller, M., Gehring, A.P., Monteiro, O.P., Martin, S.P., Fedorov, O., Heer, J., Dixon, D.J., Elkins, J.M., et al. (2018). Discovery of a novel allosteric inhibitor scaffold for polyadenosine-diphosphate-ribose polymerase 14 (PARP14) macromodulator 2. *Bioorg. Med. Chem.* *26*, 2965–2972.
- Noy, R., and Pollard, J.W. (2014). Tumor-associated macrophages: from mechanisms to therapy. *Immunity* *41*, 49–61.
- Page, M., Krehling, J., and Altiock, S. (2018). Innovative combinatorial approach to characterize the immune landscape and analyze the tumor response after anti-PD-1 blockade in a 3D ex-vivo tumoroid system of non-small cell lung cancer. *J. Immunother. Cancer* *6*, 114.
- Pathria, P., Louis, T.L., and Varner, J.A. (2019). Targeting tumor-associated macrophages in cancer. *Trends Immunol.* *40*, 310–327.
- Pechkovsky, D.V., Prasse, A., Kollert, F., Engel, K.M., Dentler, J., Luttmann, W., Friedrich, K., Muller-Quernheim, J., and Zissel, G. (2010). Alternatively activated alveolar macrophages in pulmonary fibrosis-mediator production and intracellular signal transduction. *Clin. Immunol.* *137*, 89–101.
- Peng, B., Thorsell, A.G., Karlberg, T., Schuler, H., and Yao, S.Q. (2017). Small molecule microarray based discovery of PARP14 inhibitors. *Angew. Chem. Int. Ed.* *56*, 248–253.
- Rusinova, I., Forster, S., Yu, S., Kannan, A., Masse, M., Cumming, H., Chapman, R., and Hertzog, P.J. (2013). Interferome v2.0: an updated database of annotated interferon-regulated genes. *Nucleic Acids Res.* *41*, D1040–D1046.
- Santoni, M., Massari, F., Di Nunno, V., Conti, A., Cimadamore, A., Scarpelli, M., Montironi, R., Cheng, L., Battelli, N., and Lopez-Beltran, A. (2018). Immunotherapy in renal cell carcinoma: latest evidence and clinical implications. *Drugs Context* *7*, 212528.
- Scaltriti, M., Verma, C., Guzman, M., Jimenez, J., Parra, J.L., Pedersen, K., Smith, D.J., Landolfi, S., Ramon Y Cajal, S., Arribas, J., and Baselga, J. (2009). Lapatinib, a HER2 tyrosine kinase inhibitor, induces stabilization and accumulation of HER2 and potentiates trastuzumab-dependent cell cytotoxicity. *Oncogene* *28*, 803–814.
- Schuller, M., Riedel, K., Gibbs-Seymour, I., Uth, K., Sieg, C., Gehring, A.P., Ahel, I., Bracher, F., Kessler, B.M., Elkins, J.M., and Knapp, S. (2017). Discovery of a selective allosteric inhibitor targeting macromodulator 2 of polyadenosine-diphosphate-ribose polymerase 14. *ACS Chem. Biol.* *12*, 2866–2874.
- Schulz, D., Severin, Y., Zanotelli, V.R.T., and Bodenmiller, B. (2019). In-depth characterization of monocyte-derived macrophages using a mass cytometry-based phagocytosis assay. *Sci. Rep.* *9*, 1925.
- Schweiker, S.S., Tauber, A.L., Sherry, M.E., and Levonis, S.M. (2018). Structure, function and inhibition of poly(ADP-ribose)polymerase, member 14 (PARP14). *Mini Rev. Med. Chem.* *18*, 1659–1669.
- Shapouri-Moghaddam, A., Mohammadian, S., Vazini, H., Taghadosi, M., Esmaeili, S.A., Mardani, F., Seifi, B., Mohammadi, A., Afshari, J.T., and Sahebkar, A. (2018). Macrophage plasticity, polarization, and function in health and disease. *J. Cell Physiol.* *233*, 6425–6440.
- Steenport, M., Khan, K.M., Du, B., Barnhard, S.E., Dannenberg, A.J., and Falcone, D.J. (2009). Matrix metalloproteinase (MMP)-1 and MMP-3 induce macrophage MMP-9: evidence for the role of TNF-alpha and cyclooxygenase-2. *J. Immunol.* *183*, 8119–8127.
- Thorsell, A.G., Ekblad, T., Karlberg, T., Low, M., Pinto, A.F., Tresaugues, L., Moche, M., Cohen, M.S., and Schuler, H. (2017). Structural basis for potency and promiscuity in poly(ADP-ribose) polymerase (PARP) and tankyrase inhibitors. *J. Med. Chem.* *60*, 1262–1271.

Upton, K., Meyers, M., Thorsell, A.G., Karlberg, T., Holechek, J., Lease, R., Schey, G., Wolf, E., Lucente, A., Schuler, H., and Ferraris, D. (2017). Design and synthesis of potent inhibitors of the mono(ADP-ribosyl)transferase, PARP14. *Bioorg. Med. Chem. Lett.* *27*, 2907–2911.

Viola, A., Munari, F., Sanchez-Rodriguez, R., Scolaro, T., and Castegna, A. (2019). The metabolic signature of macrophage responses. *Front. Immunol.* *10*, 1462.

Vyas, S., and Chang, P. (2014). New PARP targets for cancer therapy. *Nat. Rev. Cancer* *14*, 502–509.

Vyas, S., Matic, I., Uchima, L., Rood, J., Zaja, R., Hay, R.T., Ahel, I., and Chang, P. (2014). Family-wide analysis of poly(ADP-ribose) polymerase activity. *Nat. Commun.* *5*, 4426.

Wahlberg, E., Karlberg, T., Kouznetsova, E., Markova, N., Macchiarulo, A., Thorsell, A.G., Pol, E., Frostell, A., Ekblad, T., Oncu, D., et al. (2012). Family-wide chemical profiling and structural analysis of PARP and tankyrase inhibitors. *Nat. Biotechnol.* *30*, 283–288.

Wang, P., Li, J., Jiang, X., Liu, Z., Ye, N., Xu, Y., Yang, G., Xu, Y., and Zhang, A. (2014). Palladium-catalyzed N-arylation of 2-aminobenzothiazole-4-carboxylates/carboxamides: facile synthesis of PARP14 inhibitors. *Tetrahedron* *70*, 5666–5673.

Wigle, T., Blackwell, D.J., Schenkel, L.B., Ren, Y., Church, W.D., Desai, H.J., Swinger, K.K., Santospago, A.G., Majer, C.R., Lu, A.Z., et al. (2020). In vitro and cellular probes to study PARP enzyme target engagement. *Cell Chem. Biol.* *27*, 877–887.e14.

Wigle, T.J., Church, W.D., Majer, C.R., Swinger, K.K., Aybar, D., Schenkel, L.B., Vasbinder, M.M., Brendes, A., Beck, C., Prahm, M., et al. (2019). Forced self-modification assays as a strategy to screen MonoPARP enzymes. *SLAS Discov.* *25*, 241–252.

Witten, D.M. (2011). Classification and clustering of sequencing data using a Poisson model. *Ann. Appl. Stat.* *5*, 2493–2518.

Yoneyama-Hirozane, M., Matsumoto, S.I., Toyoda, Y., Saikatendu, K.S., Zama, Y., Yonemori, K., Oonishi, M., Ishii, T., and Kawamoto, T. (2017). Identification of PARP14 inhibitors using novel methods for detecting auto-riboseylation. *Biochem. Biophys. Res. Commun.* *486*, 626–631.

Yu, G., Wang, L.G., Han, Y., and He, Q.Y. (2012). clusterProfiler: an R package for comparing biological themes among gene clusters. *OMICS* *16*, 284–287.

Zhang, J.H., Chung, T.D., and Oldenburg, K.R. (1999). A simple statistical parameter for use in evaluation and validation of high throughput screening assays. *J. Biomol. Screen* *4*, 67–73.

STAR★METHODS

Detailed methods are provided in the online version of this paper and include the following:

KEY RESOURCES TABLE

REAGENT or RESOURCE	SOURCE	IDENTIFIER
Antibodies		
PARP14 antibody clone 15A6-1 (for Western blotting)	Genscript	U9897EA250-9
PARP14 antibody clone 15B10-1 (for immunoprecipitation)	Genscript	U0106DJ020-2
Beta-Actin	Cell Signaling Technologies	Cat#8457; RRID: AB_10950489
Phospho-STAT6	Cell Signaling Technologies	Cat#9361; RRID: AB_331595
STAT6	Cell Signaling Technologies	Cat#9362; RRID: AB_2271211
Biological Samples		
Leukopak	STEMCELL Technologies	Cat#70500.2
Human recombinant M-CSF	STEMCELL Technologies	Cat#78057
Mouse recombinant IFN-gamma	Peprtech	Cat#31505
Human recombinant IFN-gamma	STEMCELL Technologies	Cat#78020
Human recombinant IL-4	STEMCELL Technologies	Cat#78045
Human recombinant IL-13	STEMCELL Technologies	Cat#78029
Chemicals, Peptides, and Recombinant Proteins		
PARP1 (human, full-length)	Wigle et al., <i>SLAS Discovery</i> (2019)	N/A
PARP2 (human, full-length)	Wigle et al., <i>SLAS Discovery</i> (2019)	N/A
PARP3 (human, full-length)	Wigle et al., <i>SLAS Discovery</i> (2019)	N/A
PARP4 (human, truncate)	Wigle et al., <i>SLAS Discovery</i> (2019)	N/A
PARP5a (human, truncate)	Wigle et al., <i>SLAS Discovery</i> (2019)	N/A
PARP6 (human, truncate)	Wigle et al., <i>SLAS Discovery</i> (2019)	N/A
PARP7 (human, truncate)	Wigle et al., <i>SLAS Discovery</i> (2019)	N/A
PARP8 (human, truncate)	Wigle et al., <i>SLAS Discovery</i> (2019)	N/A
PARP9 (human, full-length)	Wigle et al., <i>SLAS Discovery</i> (2019)	N/A
PARP10 (human, truncate)	Wigle et al., <i>SLAS Discovery</i> (2019)	N/A
PARP11 (human, full-length)	Wigle et al., <i>SLAS Discovery</i> (2019)	N/A
PARP12 (human, truncate)	Wigle et al., <i>SLAS Discovery</i> (2019)	N/A
PARP13 (human, full-length)	Wigle et al., <i>SLAS Discovery</i> (2019)	N/A
PARP14 (human, truncate)	Wigle et al., <i>SLAS Discovery</i> (2019)	N/A
PARP14 (human, full-length)	This paper	N/A
PARP14 (mouse, truncate)	This paper	N/A
PARP14 (mouse, full-length)	This paper	N/A
PARP15 (human, truncate)	Wigle et al., <i>SLAS Discovery</i> (2019)	N/A
PARP16 (human, full-length)	Wigle et al., <i>SLAS Discovery</i> (2019)	N/A
RBN010860	Wigle et al., <i>Cell Chem Biol</i> (2020)	N/A
RBN011198	Wigle et al., <i>Cell Chem Biol</i> (2020)	N/A
RBN012759 (Compound 1)	This paper	N/A
Compound 2	This paper	N/A
Compound 3	This paper	N/A
Compound 4	This paper	N/A
Biotin-NAD ⁺	Biolog	Cat#N012
Doxycycline	Millipore Sigma	Cat#D3072
HEPES pH = 7.5	Alfa Aesar	Cat#J60712

(Continued on next page)

Continued

REAGENT or RESOURCE	SOURCE	IDENTIFIER
NaCl	Quality Biological	Cat#351-036-721
Tween 20	Thermo	Cat#28320
DPTA-purified BSA	Perkin Elmer	Cat#CR84-100
Dithiothreitol	Fisher Scientific	Cat#BP172-25
TBS-T	Hoefler	Cat#GR154-1
PBS-T	Boston Bioproducts	Cat#IBB-645
Methanol	Fisher Scientific	Cat#A412-1
DMSO	Millipore Sigma	Cat#D8418
MEM + Glutamax media	Thermo	Cat#41090036
OptiMEM media	Thermo	Cat#11058021
DMEM media	Thermo	Cat#10569010
Fetal bovine serum	VWR	Cat#97068-085
FuGENE(R) HD Transfection Reagent	Promega	Cat#E2312
Methylcellulose	Sigma-Aldrich	Cat#M7027-250G
Tween 80	Shanghai Titan Scientific Co. Ltd	Cat#G8919113

Critical Commercial Assays

Europium-labeled streptavidin	Perkin Elmer	Cat#AD0063
ULight-labeled streptavidin	Perkin Elmer	Cat#AD0062
Europium-labeled anti-His	Perkin Elmer	Cat#AD0111
Ulight-labeled anti-His	Perkin Elmer	Cat#TRF0105
384-well nickel-NTA coated microplates	Thermo	Custom
DELFI Eu-N1 Streptavidin	Perkin Elmer	Cat#1244-360
DELFI Assay Buffer	Perkin Elmer	Cat#1244-111
DELFI Enhancement Solution	Perkin Elmer	Cat#1244-105
IntracellularTE Nano-Glo(R) Substrate/Inhibitor	Promega	Cat#N2161
IL-10 quantikine ELISA kit	R&D systems	Cat#D1000B
Luminex Cytokine Human 25-Plex Panel	Invitrogen	Cat#LHC0009
RIPA lysis buffer	Millipore	Cat#20-188
SDS	Amresco	Cat#E719
HALT protease/phosphatase inhibitor	ThermoFisher	Cat#23225
Sample buffer	LICOR	Cat#92840004
PVDF membranes	ThermoFisher	Cat#IB24001
MOPS running buffer	ThermoFisher	Cat#NP0001
4-12% Bis-Tris gels	BIORAD	Cat#3450124
Blocking buffer	LICOR	Cat#92632213
TRI reagent	ThermoFisher	Cat#AM9738
PanCancer IO 360™ Panel	nanoString	Cat#PanCancer IO 360™ Panel
QIAshredder columns	QIAGEN	Cat#79565
Mag MAX kit	Ambio	Cat#1830M
TRIxol reagent	Invitrogen	Cat#15596018

Deposited Data

Structure of PARP14 bound to Compound 2	This paper	PDB: 6WE4
Structure of PARP14 bound to Compound 3	This paper	PDB: 6WE3
Structure of PARP14 bound to RBN012759	This paper	PDB: 6WE2

Experimental Models: Cell Lines

293T cells	ATCC	Cat#CRL-3216
RAW264.7 cells	ATCC	Cat#TIB-71™
CFPAC-1 cells	ATCC	Cat# CRL-1918

(Continued on next page)

Continued

REAGENT or RESOURCE	SOURCE	IDENTIFIER
Experimental Models: Organisms/Strains		
Mus Musculus / C57BL/6	Shanghai Lingchang BioTech	N/A
Oligonucleotides		
Activating dsDNA for PARP1 (5' ACCCTGCTGTGG GC/ideoxyU/GGAGAACAAGGTGAT and 3' ATCACCTTGTCTCCAAGCCACAGCAGGGT)	IDT DNA	N/A
Activating dsDNA for PARP2 (5'/phosphate/GCCTATAGGC and 3'/phosphate/GCCTATACCG)	IDT DNA	N/A
Activating ssDNA for PARP3 (/phosphate/GCTG GCTTCGTAAGAAGCCAGCTCGCGGTCAGC TTGCTGACCGCG)	IDT DNA	N/A
Recombinant DNA		
pcDNA3.1 plasmid		
pcDNA3.1 with human PARP1 amino acids 1-1014 with C-terminal or N-terminal NanoLuc tag	Wigle et al., <i>Cell Chem Biol</i> (2020)	N/A
pcDNA3.1 with human PARP3 amino acids 1 – 533 with C-terminal or N-terminal NanoLuc tag	Wigle et al., <i>Cell Chem Biol</i> (2020)	N/A
pcDNA3.1 with human PARP7 amino acids 1-657 insert with C-terminal or N-terminal NanoLuc tag	Wigle et al., <i>Cell Chem Biol</i> (2020)	N/A
pcDNA3.1 with human PARP7 amino acids 456-657 insert with C-terminal or N-terminal NanoLuc tag	Wigle et al., <i>Cell Chem Biol</i> (2020)	N/A
pcDNA3.1 with human PARP10 amino acids 808-1025 with C-terminal or N-terminal NanoLuc tag	Wigle et al., <i>Cell Chem Biol</i> (2020)	N/A
pcDNA3.1 with human PARP10 amino acids 1-1025 with C-terminal or N-terminal NanoLuc tag	Wigle et al., <i>Cell Chem Biol</i> (2020)	N/A
pcDNA3.1 with human PARP11 amino acids 1-338 with C-terminal or N-terminal NanoLuc tag	Wigle et al., <i>Cell Chem Biol</i> (2020)	N/A
pcDNA3.1 with human PARP12 amino acids 1-701 with C-terminal or N-terminal NanoLuc tag	Wigle et al., <i>Cell Chem Biol</i> (2020)	N/A
pcDNA3.1 with human PARP14 amino acids 1611-1801 with C-terminal or N-terminal NanoLuc tag	Wigle et al., <i>Cell Chem Biol</i> (2020)	N/A
pcDNA3.1 with human PARP14 amino acids 1-1801 with C-terminal or N-terminal NanoLuc tag	Wigle et al., <i>Cell Chem Biol</i> (2020)	N/A
pcDNA3.1 with human PARP16 amino acids 1-322 with C-terminal or N-terminal NanoLuc tag	Wigle et al., <i>Cell Chem Biol</i> (2020)	N/A
Software and Algorithms		
Odyssey Image Studio	Licor https://www.licor.com/bio/image-studio/	N/A
R statistical software	r-project.org	Version 3.6.1
DESeq2	Love et al., <i>Genome Biol</i> (2014) https://bioconductor.org/packages/release/bioc/html/DESeq2.html	Version 1.18.17
Salmon	Patro et al., <i>Nat Meth</i> (2017) https://combine-lab.github.io/salmon/	Version 0.11.26
ComplexHeatmap	Gu et al., <i>Bioinformatics</i> (2016) http://bioconductor.org/packages/release/bioc/html/ComplexHeatmap.html	Version 2.2.0

(Continued on next page)

Continued

REAGENT or RESOURCE	SOURCE	IDENTIFIER
Other		
Envision platereader	Perkin Elmer	Cat#2101-0010
Biacore T200 SPR instrument	GE Healthcare	Cat#28975001
Streptavidin SPR chips	GE Healthcare	Cat#29104992
NTA SPR chips	GE Healthcare	Cat#28994951
Odyssey CLX infrared imager	Licor	Cat. # 9140
BioRad BioPlex MAGPIX multilex reader system	BioRad	Cat#171000201
BioRad TransBLot Turbo Transfer system	BioRad	Cat#1704150

RESOURCE AVAILABILITY

Lead contact

Further information and requests for reagents and resources should be directed to the lead contact, Kevin W. Kuntz (kkuntz@ribontx.com).

Materials availability

Reagents generated in this study are available from the Lead Contact with a completed Materials Transfer Agreement.

Data code and availability

The coordinates for the protein structures reported in this manuscript have been deposited in Protein Data Bank (<http://rcsb.org/pdb>) under ID codes 6WE4, 6WE3, and 6WE2.

EXPERIMENTAL MODEL

Cell lines

293T cells (ATCC; sex: female) expressing PARP-NanoLuc fusion proteins, RAW 267.4 cells (ATCC; sex: male), and CFPAC-1 cells (ATCC; sex: male) were grown in Dulbecco's modified Eagle's medium (DMEM) supplemented with 10% heat inactivated fetal bovine serum (VWR) in a 5% CO₂ environment at 37°C.

In vivo animal studies

All procedures related to animal handling, care and treatment were performed according to the guidelines approved by the Institutional Animal Care and Use Committee (IACUC) following the guidance of the Association for Assessment and Accreditation of Laboratory Animal Care (AAALAC). For the pharmacokinetics studies, male CD1 mice were obtained from the Animal Facility of Beijing Vital River Laboratory Animal Technology Co., Ltd. For the *in vivo* target engagement studies, C57Bl/6 J female mice were obtained from Shanghai Lingchang BioTech Co., Ltd. All mice were kept in individual ventilation cages under a 12 hour light/dark cycle with free access to food and water at constant temperature (20–25°C) and humidity (40–70%), and with 3 or 5 animals in each cage. Mice were between 6 to 8 weeks of age, weighed 20–25 g (male CD1 mice) and 18–20 g (female C57Bl/6 mice), and were randomly assigned to experimental groups.

METHOD DETAILS

Assay and chemistry reagents

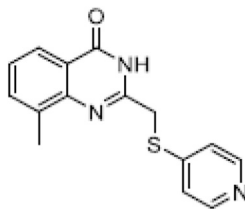
TR-FRET reagents used in the *in vitro* active site probe displacement TR-FRET assays, DELFIA reagents used in the self-modification enzyme assays and 384-well proxiplates were purchased from Perkin Elmer. NaCl, HEPES, 384-well PCR microplates and thermal shift dye were purchased from VWR. Tween-20, dithiothreitol (DTT) and 384-well nickel-NTA coated microplates were purchased from Thermo Fisher Scientific. Tris-buffered saline was purchased from Hoefer. NAD⁺ was purchased from Millipore-Sigma. Biotin-NAD⁺ was purchased from BIOLOG Life Sciences Institute. All reactions were carried out in commercially available glassware using standard synthetic chemistry methods, and reagents were purchased commercially and used without further purification. RBN010860 and RBN011198 were prepared as previously described ([Wigle et al., 2020](#)).

Chemistry

List of abbreviations:

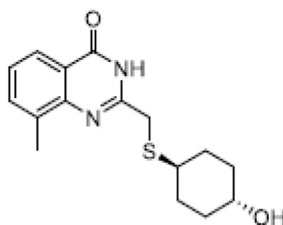
ACN (acetonitrile); DCM (dichloromethane); DMSO (dimethylsulfoxide); EtOAc (ethyl acetate); g (gram); h (hours); HRMS (high resolution mass spectrometry); LCMS (liquid chromatography-mass spectrometry); MeOH (methanol); MHz (megahertz); mL (milliliter); mmol (millimole); NMP (*N*-methyl-2-pyrrolidinone); NMR (nuclear magnetic resonance); RT (room temperature); THF (tetrahydrofuran); TFA (trifluoroacetic acid); TLC (thin layer chromatography)

Synthesis of 8-methyl-2-((pyridin-4-ylthio)methyl)quinazolin-4(3H)-one (2):



A mixture of 2-(chloromethyl)-8-methylquinazolin-4(3H)-one (300 mg, 1.44 mmol, 1.0 equiv), pyridine-4-thiol (190 mg, 1.73 mmol, 1.2 equiv), NaI (216 mg, 1.44 mmol, 1.0 equiv), and Cs₂CO₃ (1.41 g, 4.32 mmol, 3.0 equiv) in 25 mL acetone was heated at reflux for 2 h under an atmosphere of nitrogen. The mixture was diluted with 100 mL water and extracted with EtOAc (2 x 100 mL). The combined organic portion was washed with 100 mL brine, dried over Na₂SO₄, and concentrated under reduced pressure. The crude material was purified by preparative TLC using 20:1 DCM:MeOH to give the title compound as a yellow solid (200 mg, 49%). LCMS: [M+H]⁺ 284.1; ¹H NMR (400 MHz, DMSO-*d*₆) δ 12.43 (s, 1H), 8.40 (d, *J* = 6.0, 2H), 7.92 (d, *J* = 7.2, 1H), 7.64 (d, *J* = 5.2, 1H), 7.55-7.54 (m, 2H), 7.39-7.35 (m, 1H), 4.30 (s, 2H), 2.48 (s, 3H); ¹³C NMR (100.5 MHz, DMSO-*d*₆) δ 162.26, 152.44, 149.51, 147.77, 147.10, 135.58, 135.32, 126.64, 123.86, 121.48, 121.36, 33.94, 17.45; HRMS: [M+H]⁺ Calcd for C₁₅H₁₄N₃OS 284.0858; found 284.0858.

C



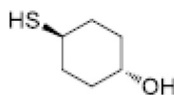
LCMS: [M+H]⁺ 305.1;

¹H NMR (400 MHz, DMSO-*d*₆) δ 12.27 (s, 1H), 7.95 – 7.93 (m, 1H), 7.67 (d, *J* = 6.8 Hz, 1H), 7.38 (t, *J* = 7.6 Hz, 1H), 4.55 (d, *J* = 4.4 Hz, 1H), 3.64 (s, 2H), 3.39 – 3.34 (m, 1H), 2.82 – 2.75 (m, 1H), 2.51 (s, 3H), 2.02 (d, *J* = 12.3 Hz, 2H), 1.83 (d, *J* = 12.0 Hz, 2H), 1.28 – 1.19 (m, 4H).

¹³C NMR (400 MHz, DMSO-*d*₆) δ 162.543 (1C), 154.250 (1C), 147.471 (1C), 135.433 (1C), 135.194 (1C), 126.242 (1C), 123.872 (1C), 121.252 (1C), 68.455 (1C), 42.294 (1C), 35.463 (1C), 33.137 (1C), 31.216 (2C), 17.549 (2C). HRMS: [M+H]⁺ Calcd for C₁₆H₂₀N₂O₂S 305.1324; found 305.1312.

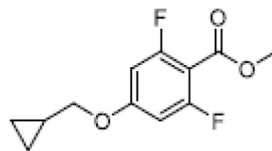
Synthesis of 7-(cyclopropylmethoxy)-5-fluoro-2-(((1r,4r)-4-hydroxycyclohexyl)thio)methyl)quinazolin-4(3H)-one (RBN012759):

trans-4-Mercaptocyclohexanol.



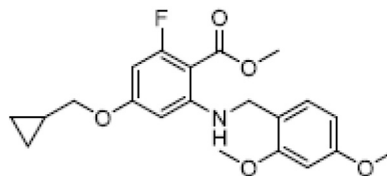
To a solution 7-oxabicyclo[2.2.1]heptane (1 g, 10.2 mmol, 1.0 eq) in ethanol (10 mL) was added *p*-TSA (2.91g, 15.3mmol) and thio-urea (1.2 g, 15.8 mmol, 1.5 eq) and the mixture was heated at reflux for 21 h. After cooling to RT, NaOH (1.3 g) and water (3 mL) were added and the solution was heated at reflux for a further 2 h. The mixture was cooled to RT, NaOH (1.3 g) and water (3 mL) were added and the solution was heated at reflux for a further 2 h, then allowed to cool to RT and concentrated under reduced pressure. The residue was diluted with water (15 mL) and adjusted to pH 3–4 with 1 M HCl and extracted with EtOAc (50 mL x 3). The combined organic layers were washed with brine (50 mL), dried over Na₂SO₄ and concentrated under reduced pressure. The residue was purified by column chromatography (Petroleum ether:EtOAc, 10:1, v/v) to afford the title compound (500 mg, 37%) as a yellow oil. ¹H NMR (400 MHz, DMSO-*d*₆) δ 6.18 (br s, 1H), 4.51 (br s, 1H), 3.41 – 3.36 (m, 1H), 2.73 – 2.64 (m, 1H), 1.96 – 1.86 (m, 2H), 1.72 – 1.81 (m, 2H), 1.36 – 1.26 (m, 2H), 1.23 – 1.17 (m, 2H).

Methyl 4-(cyclopropylmethoxy)-2,6-difluorobenzoate.



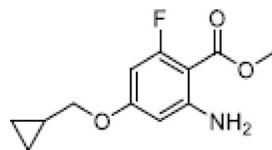
A mixture of methyl 2,6-difluoro-4-hydroxybenzoate, (bromomethyl)cyclopropane (102 mL, 1.05 mol) and K_2CO_3 (330 g, 2.39 mol) in DMSO (1 L) was heated at 80°C overnight. The mixture was diluted with water (5 L) and extracted with EtOAc (1 L x 3). The combined organic extracts were washed with water (800 mL), brine (800 mL), dried over Na_2SO_4 and concentrated under reduced pressure to afford the title compound (214 g, 92%) as a brown oil. LCMS: $[M+H]^+$ 243.1.

Methyl 4-(cyclopropylmethoxy)-2-((2,4-dimethoxybenzyl)amino)-6-fluorobenzoate.



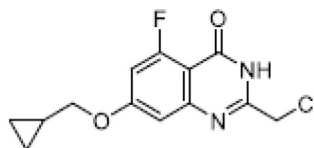
A mixture of methyl 4-(cyclopropylmethoxy)-2,6-difluorobenzoate (214 g, 881 mmol), (2,4-dimethoxyphenyl)methanamine (139 mL, 926 mmol) and K_2CO_3 (243 g, 1.76 mol) in NMP (1 L) was heated at 80°C overnight. The mixture was poured into water (5 L), and the resulting precipitate was collected by filtration and washed with water (800 mL). The filter cake was dissolved in DCM (2.5 L) and washed with brine (800 mL). The organic layer was dried over Na_2SO_4 and concentrated under reduced pressure to give the title compound (343 g, 99%) as an off-white solid. LCMS: $[M+Na]^+$ 412.1.

Methyl 2-amino-4-(cyclopropylmethoxy)-6-fluorobenzoate.



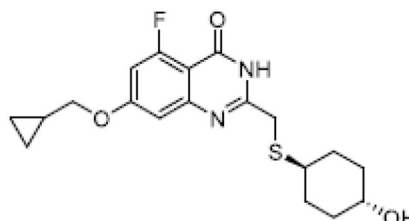
To a solution of methyl 4-(cyclopropylmethoxy)-2-((2,4-dimethoxybenzyl)amino)-6-fluorobenzoate (1.6 g, 4.11 mmol, 1.0 eq) in DCM (8.0 mL) was added TFA (4.0 mL) and the mixture was stirred at RT for 2 h. The mixture was concentrated under reduced pressure and the residue was purified by column chromatography (DCM:MeOH, 20/1, v/v) to afford the title compound (0.9 g, 91%) as a brown solid. LCMS: $[M+H]^+$ 240.1.

2-(Chloromethyl)-7-(cyclopropylmethoxy)-5-fluoroquinazolin-4(3H)-one



To a solution of methyl 2-amino-4-(cyclopropylmethoxy)-6-fluorobenzoate (900 mg, 3.76 mmol, 1 equiv) in 4 M HCl/dioxane (8 mL, 32 mmol, 8.51 equiv) was added 2-chloroacetonitrile (1.19 mL, 18.8 mmol, 5 equiv). The mixture was heated at 80°C for 3 h. The mixture was concentrated and purified by silica gel column (DCM/MeOH = 40/1, v/v) to afford the title compound (600 mg, 2.12 mmol, 56% yield) as a white solid. LCMS: $[M+H]^+$ 283.1.

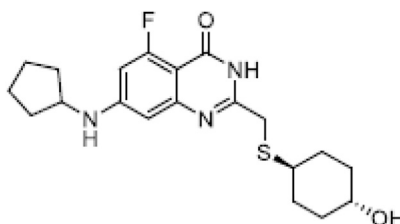
7-(Cyclopropylmethoxy)-5-fluoro-2-(((trans-4-hydroxycyclohexyl)thio)methyl)quinazolin-4(3H)-one.



To a solution of 2-(chloromethyl)-7-(cyclopropylmethoxy)-5-fluoroquinazolin-4(3H)-one (300 mg, 1.06 mmol, 1.0 eq) in THF (5 mL) under a N₂ atmosphere was added trans-4-mercaptocyclohexanol (168 mg, 1.27 mmol, 1.2 eq) and 2 M NaOH (2 mL) and the mixture was stirred at RT overnight. The mixture was poured into water (30 mL) and extracted with EtOAc (20 mL x 3). The combined organic layers were washed with brine (30 mL), dried over Na₂SO₄ and concentrated under reduced pressure. The residue was purified by C18 reverse phase column (Biotage, 40% ACN in water) to afford the title compound (130 mg, 32%) as a white solid. LCMS: [M+H]⁺ 379.1; ¹H NMR (400 MHz, DMSO-*d*₆) δ 12.1 (s, 1H), 6.89-6.86 (m, 2H), 4.52 (d, *J* = 4.4 Hz, 1H), 3.96 (d, *J* = 7.2 Hz, 2H), 3.57 (s, 2H), 3.40-3.38 (m, 1H), 2.74-2.67 (m, 1H), 1.97-1.94 (m, 2H), 1.82-1.80 (m, 2H), 1.28-1.11 (m, 5H), 0.60-0.58 (m, 2H), 0.37-0.33 (m, 2H); ¹³C NMR (400 MHz, DMSO-*d*₆) δ 163.841 (d, *J* = 14.1 Hz, 1C), 162.076 (d, *J* = 259.5 Hz, 1C), 159.080 (d, *J* = 2.9 Hz, 1C), 157.199 (1C), 152.549 (1C), 106.176 (d, *J* = 2.4 Hz, 1C), 104.392 (d, *J* = 7.1 Hz, 1C), 102.798 (d, *J* = 23.4 Hz, 1C), 73.580 (1C), 68.320 (1C), 42.737 (1C), 35.276 (1C), 33.211 (2C), 31.401 (2C), 10.276 (1C), 3.622 (2C).

HRMS: [M+H]⁺ Calcd for C₁₉H₂₃FN₂O₃S 379.1492; found 379.1493.

Synthesis of 7-(Cyclopentylamino)-2-(((trans-4-hydroxycyclohexyl)thio)methyl) quinazolin-4(3H)-one (4) was carried out following the procedures detailed in PCT Int. Appl. (2019) WO 2019126443 A1 20190627



LCMS: [M+H]⁺ 374.2; ¹H NMR (400 MHz, DMSO-*d*₆) δ 11.6 (br s, 1H), 7.70 (d, *J* = 8.0 Hz, 1H), 6.69 (dd, *J* = 8.0, 2.0 Hz, 1H), 6.50 (m, 1H), 6.45 (d, *J* = 2.0 Hz, 1H), 4.52 (br s, 1H), 3.74 - 3.82 (m, 1H), 3.52 (s, 2H), 3.39 - 3.35 (m, 1H), 2.76 - 2.64 (m, 1H), 2.03 - 1.90 (m, 4H), 1.82 - 1.76 (m, 2H), 1.73 - 1.63 (m, 2H), 1.62 - 1.53 (m, 2H), 1.52 - 1.42 (m, 2H), 1.24 - 1.13 (m, 4H); ¹³C NMR (300 MHz, DMSO-*d*₆) δ 162.214 (d, *J* = 128 Hz, 1C), 159.076 (d, *J* = 1.65 Hz, 1C), 156.248 (1C), 153.866 (d, *J* = 6.90 Hz, 1C), 152.443 (1C), 102.306 (1C), 99.510 (1C), 99.253 (d, *J* = 3.98 Hz, 1C), 68.344 (1C), 53.801 (1C), 42.735 (1C), 35.342 (2C), 33.215 (1C), 32.716 (2C), 31.432 (2C), 24.105 (2C). HRMS: [M+H]⁺ Calcd for C₂₀H₂₆FN₃O₃S 392.1808; found 392.1802.

Protein purification and crystallography

Recombinant enzymes were expressed and purified as described previously. PARP14 (NM_017554, human and NM_001039530.3, mouse) recombinant proteins were purified by the same method using an N-terminal hexahistidine (His6) tag (Wigle et al., 2019).

PARP1 (NP_001609.2), amino acids 1 - 1014, was cloned into a pFastBac1 insect expression vector with N-terminal FLAG and hexahistidine tags, with a tobacco etch virus (TEV) cleavage site between the FLAG tag and the His tag. PARP1 was expressed in Sf9 insect cells and harvested at 48 h. The cells were resuspended in lysis buffer (20 mmol/L 2-amino-2-(hydroxymethyl)propane-1,3-diol (Tris)-HCl (pH = 7.5), 200 mmol/L sodium chloride (NaCl), 5% glycerol, 5 mmol/L beta-mercaptoethanol) and lysed by sonication. The protein was purified by nickel-nitrilotriacetic acid (Ni-NTA) affinity gel chromatography and anti-FLAG affinity gel chromatography and stored in 20 mmol/L Tris-HCl (pH = 7.5), 200 mmol/L NaCl, 5 mmol/L beta-mercaptoethanol and 5% glycerol.

PARP2 (NP_005475.2), amino acids 1 - 583, was cloned into a pFastBac1 insect expression vector with N-terminal FLAG and hexahistidine tags, and a TEV cleavage site between the FLAG tag and the His tag. PARP2 was expressed in Sf9 insect cells and harvested at 48 h. The cells were resuspended in lysis buffer (25 mmol/L 4-(2-hydroxyethyl)-1-piperazineethanesulfonic acid (HEPES) (pH = 7.5), 500 mmol/L NaCl, 10% glycerol, 1 mmol/L Tris(2-carboxyethyl)phosphine (TCEP), 10 mmol/L magnesium chloride (MgCl₂) and 1 unit/mL DNase) and lysed by sonication. The protein was purified by anti-FLAG affinity gel chromatography and stored in 25 mmol/L HEPES (pH = 7.5), 300 mmol/L NaCl, 1 mmol/L TCEP, 200 μg/mL FLAG peptide and 10% glycerol.

PARP3 (NP_001003931.3) amino acids 1 - 533 was cloned into pTrilJ-HV expression vector with an N-terminal hexahistidine tag followed by a TEV cleavage site, streptavidin binding protein (SBP) sequence and PreScission protease (PRX) cleavage site. The protein was expressed in Sf21 insect cells and harvested at 72 h. Cells were resuspended in lysis buffer (25 mmol/L Tris-HCl (pH = 8), 300 mmol/L NaCl, 5% glycerol, 1 mmol/L TCEP, 1X Roche protease inhibitor cocktail, 1 mmol/L phenylmethylsulfonyl fluoride (PMSF), 10 units/mL benzonase, and 0.25% 3-[[3-Cholamidopropyl] dimethylammonio]-1-propanesulfonate (CHAPS)) and lysed by sonication. The protein was purified by Ni-NTA affinity chromatography, followed by S-200 size exclusion chromatography. Purified protein was stored in 25 mmol/L Tris-HCl (pH = 7.5), 300 mmol/L NaCl, 1 mmol/L TCEP and 5% glycerol.

PARP4 (NP_006428.2) amino acids 226 - 566 was cloned into pTrilJ-HV expression vector with an N-terminal hexahistidine tag, and a TEV cleavage site and glycine residue between the hexahistidine tag and the gene. The protein was expressed in Sf21 insect cells and harvested at 72 h. Cells were resuspended in lysis buffer (25 mmol/L Tris-HCl (pH = 7.5), 300 mmol/L NaCl, 5% glycerol, 1 mmol/L TCEP, 1X Roche protease inhibitor cocktail, 1 mmol/L PMSF, 10 units/mL and 0.25% CHAPS) and lysed by sonication. The

protein was purified by Ni-NTA affinity chromatography, followed by S-200 size exclusion chromatography. Purified protein was stored in 25 mmol/L Tris-HCl (pH = 7.5), 300 mmol/L NaCl, 1 mmol/L TCEP and 5% glycerol.

PARP5b (NM_025235) amino acid 667 – 1166 was purchased from BPS Biosciences (catalog #80505). The protein construct contained an N-terminal glutathione S-transferase (GST) tag and was expressed and purified from Sf9 insect cells, then was stored in 40 mmol/L Tris-HCl (pH 8), 210 mmol/L NaCl, 2.2 mmol/L potassium chloride (KCl), 0.04% Tween20, 3 mmol/L dithiothreitol (DTT) and 20% glycerol.

PARP6 (NP_001310451.1) amino acids 321 – 630 was cloned into pTriJ-HV expression vector with an N-terminal hexahistidine tag. The protein was expressed in *E. coli* BL21-Gold(DE3) cells by addition of 0.5 mmol/L isopropyl β -D-1-thiogalactopyranoside (IPTG) for 16 h at 16°C. Cells were resuspended in lysis buffer (20 mmol/L Tris-HCl (pH = 7.5), 300 mmol/L NaCl, 5% glycerol, 1 mmol/L TCEP and 1X Roche protease inhibitor cocktail) and lysed by sonication. The protein was purified by Ni-NTA affinity chromatography followed by cation exchange and S-200 size exclusion chromatography. Purified protein was stored in 25 mmol/L Tris-HCl (pH = 7.5), 300 mmol/L NaCl, 1 mmol/L TCEP and 5% glycerol.

PARP7 (NP_001171646.1) amino acids 456 – 657 was cloned into pET21b expression vector with N-terminal hexahistidine and Avi tags, and a TEV cleavage site between the hexahistidine and Avi tags. The protein was expressed in inclusion bodies in *E. coli* BL21-CodonPlus (DE3)-RIL cells by addition of 0.3 mmol/L IPTG for 4 h at 37°C. Cells were resuspended in lysis buffer (40 mmol/L Tris-HCl (pH = 8), 110 mmol/L NaCl, 2.2 mmol/L KCl, 5 mmol/L beta-mercaptoethanol, 1X Roche protease inhibitor cocktail and 20% glycerol) and lysed by sonication. Inclusion bodies were washed with 50 mmol/L Tris-HCl (pH 8.0), 1 mol/L urea, 500 mmol/L NaCl, 1 mmol/L Ethylenediaminetetraacetic acid (EDTA) and 0.2% (w/v) Triton X-100. The denatured protein was purified by Ni-NTA chromatography, then the protein was then refolded by dilution into 20 mmol/L Tris-HCl (pH = 7.4), 50 mmol/L NaCl, 1 mmol/L glutathione disulfide, 10 mmol/L glutathione, 200 mmol/L L-arginine, 400 mmol/L sucrose and 15% glycerol, followed by passage over a Ni-NTA column for a second time. Purified protein was stored in 20 mmol/L Tris-HCl (pH = 7.5), 200 mmol/L NaCl, 5 mmol/L beta-mercaptoethanol, 300 mmol/L imidazole and 10% glycerol.

PARP8 (NP_001171526.1) amino acids 630 – 854 was cloned into pTriJ-HV expression vector with an N-terminal hexahistidine tag. The protein was expressed in *E. coli* BL21-Gold(DE3) cells by addition of 0.5 mmol/L IPTG for 16 h at 16°C. Cells were resuspended in lysis buffer (25 mmol/L Tris-HCl (pH = 7.5), 300 mmol/L NaCl, 1 mmol/L TCEP, 0.5 % CHAPS, 10 mmol/L MgCl₂, 1 unit/mL DNase and 5% glycerol) and lysed by sonication. The protein was purified by Ni-NTA chromatography followed by cation exchange chromatography and S-200 size exclusion chromatography. Purified protein was stored in 25 mmol/L Tris-HCl (pH = 7.5), 300 mmol/L NaCl, 1 mmol/L TCEP and 5% glycerol.

PARP9 (NP_001139574.1) amino acids 1 – 854 was cloned into a pFastBac1 insect expression vector with an N-terminal maltose binding protein (MBP) tag and a TEV cleavage site between the MBP tag and the gene. DTX3L (NP_612144.1) amino acids 1 – 740 was cloned into a pFastBac1 insect expression vector with an N-terminal hexahistidine tag and a thrombin cleavage site between the hexahistidine tag and the gene. PARP9 and DTX3L were co-expressed in High Five insect cells and harvested at 48 h. Cells were resuspended in lysis buffer (20 mmol/L HEPES (pH = 7.5), 200 mmol/L NaCl, 1 mmol/L TCEP, 1X Roche protease inhibitor cocktail, 1 unit/mL DNase, 0.5% CHAPS and 5% glycerol) and lysed by passing through a high-pressure homogenizer at 200 bar then subsequently at 300 bar. The protein was purified by Ni-NTA chromatography followed by MBP chromatography. Purified protein was stored in 20 mmol/L HEPES (pH = 7.5), 200 mmol/L NaCl, 1 mmol/L TCEP and 5% glycerol.

PARP10 (NP_0011617821) amino acids 808 – 1025 was cloned into pET21b expression vector with an N-terminal hexahistidine tag and a TEV cleavage site between the hexahistidine tag and the gene. The protein was expressed in *E. coli* BL21-CodonPlus (DE3)-RIL cells by addition of 0.5 mmol/L IPTG for 18 h at 18°C. Cells were resuspended in lysis buffer (20 mmol/L HEPES (pH = 7.5), 500 mmol/L NaCl and 5 mmol/L imidazole) and lysed by sonication. The protein was purified by Ni-NTA chromatography followed by anion exchange chromatography and S-200 size exclusion chromatography. Purified protein was stored in 20 mmol/L HEPES (pH = 7.5), 200 mmol/L NaCl and 2 mmol/L TCEP.

PARP11 (NP_0001273450.1) amino acids 1 – 337 was cloned into pTriJ-HV expression vector with an N-terminal hexahistidine tag and a C-terminal MBP tag, including a TEV cleavage site between the gene and the MBP tag. The protein was expressed in Sf21 insect cells and harvested at 72 h. Cells were resuspended in lysis buffer (25 mmol/L Tris-HCl (pH = 8), 300 mmol/L NaCl, 1 mmol/L TCEP, 1X Roche protease inhibitor cocktail, 1 mmol/L PMSF, 10 unit/mL benzonase, 0.25% CHAPS and 5% glycerol) and lysed by sonication. The protein was purified by Ni-NTA affinity chromatography, then MBP chromatography, followed by S-200 size exclusion chromatography. Purified protein was stored in 25 mmol/L Tris-HCl (pH = 7.5), 300 mmol/L NaCl, 1 mmol/L TCEP and 5% glycerol.

PARP12 (NP_073587.1) amino acids 489 – 684 was cloned into pTriJ-HV expression vector with an N-terminal hexahistidine tag, plus a TEV cleavage site and residues serine and methionine between the hexahistidine tag and the gene. The protein was expressed in Sf21 insect cells and harvested at 72 h. Cells were resuspended in lysis buffer (25 mmol/L Tris-HCl (pH = 8), 300 mmol/L NaCl, 1 mmol/L TCEP, 1X Roche protease inhibitor cocktail, 1 mmol/L PMSF, 10 units/mL benzonase, 0.25% CHAPS and 5% glycerol) and lysed by sonication. The protein was purified by Ni-NTA affinity chromatography, followed by S-200 size exclusion chromatography. Purified protein was stored in 25 mmol/L Tris-HCl (pH = 7.5), 300 mmol/L NaCl, 1 mmol/L TCEP and 5% glycerol.

PARP14 (NP_060024.2) amino acids 1611 – 1801 was cloned into pET21b expression vector with an N-terminal hexahistidine tag and a TEV cleavage site between the His tag and the gene or with N-terminal hexahistidine tag, Avi tag and a TEV cleavage site between the His tag and the gene. The protein was expressed in *E. coli* BL21-CodonPlus (DE3)-RIL cells by addition of 0.5 mmol/L IPTG for 16 h at 18°C. Cells were resuspended in lysis buffer (20 mmol/L HEPES (pH = 7), 500 mmol/L NaCl, 5 mmol/L imidazole and 1X

Roche protease inhibitor cocktail) and lysed by sonication. The protein was purified by Ni-NTA chromatography, followed by S-200 size exclusion chromatography. Avi-tagged constructs were biotinylated by BirA either *in vitro* using recombinant enzyme and confirmed to have close to 100% modification via mass spectrometry. Purified protein was stored in 20 mmol/L HEPES (pH = 7.5), 200 mmol/L NaCl and 2 mmol/L TCEP.

PARP15 (NP_001106995.1) amino acids 481 – 678 was cloned into pET21b expression vector with an N-terminal hexahistidine tag, plus an additional sequence SSGVDLGT, and a TEV cleavage site between the additional sequence and the gene. The protein was expressed in *E. coli* BL21-CodonPlus (DE3)-RIL cells by addition of 0.5 mmol/L IPTG for 16 h at 18°C. Cells were resuspended in lysis buffer (25 mmol/L Tris-HCl (pH = 7.5), 300 mmol/L NaCl, 1 mmol/L TCEP, 1X Roche protease inhibitor cocktail, 1 mmol/L PMSF, 1 unit/mL DNase, 0.25% CHAPS and 5% glycerol) and lysed by sonication. The protein was purified by Ni-NTA chromatography followed by S-200 size exclusion chromatography. Purified protein was stored in 20 mmol/L HEPES (pH = 7.5), 200 mmol/L NaCl and 2 mmol/L TCEP.

PARP16 (NP_001303872.1) amino acids 5 – 279 was cloned into pET21b expression vector with an N-terminal hexahistidine tag and a TEV cleavage site between the hexahistidine tag and the gene. The protein was expressed in *E. coli* BL21-CodonPlus (DE3)-RIL cells by addition of 0.5 mmol/L IPTG for 16 h at 16°C. Cells were resuspended in lysis buffer (20 mmol/L Tris-HCl (pH = 7.5), 300 mmol/L NaCl, 1 mmol/L TCEP, 1X Roche protease inhibitor cocktail and 5% glycerol) and lysed by sonication. The protein was purified by Ni-NTA chromatography, followed by cation exchange and S-200 size exclusion chromatography. Purified protein was stored in 20 mmol/L HEPES (pH = 7.5), 300 mmol/L NaCl, 2 mmol/L TCEP and 10% glycerol.

UBA1 (NP_003325.2) amino acids 1 – 1058 was cloned into a pFastBac1 insect expression vector with an N-terminal FLAG tag. UBA1 was expressed in Sf9 insect cell lines and harvested at 48 h. The cells were resuspended in lysis buffer (20 mmol/L HEPES (pH = 7.5), 200 mmol/L NaCl, 1 mmol/L TCEP, 1X Roche protease inhibitor cocktail, 10 mmol/L MgCl₂, 1 unit/mL DNase and 5% glycerol) and lysed by sonication. Protein was purified by FLAG chromatography, followed by S-200 size exclusion chromatography. Purified protein was stored in 20 mmol/L HEPES (pH = 7.5), 200 mmol/L NaCl, 1 mmol/L TCEP and 5% glycerol.

UBE2D1 (NP_003329.1) amino acids 1 – 147 was cloned into pET21W7 expression vector with an N-terminal hexahistidine tag and a TEV cleavage site between the hexahistidine tag and the gene. The protein was expressed in *E. coli* BL21-CodonPlus (DE3)-RIL cells by addition of 0.5 mmol/L IPTG for 16 h at 16°C. Cells were resuspended in lysis buffer (25 mmol/L HEPES (pH = 7.8), 250 mmol/L NaCl, 1 mmol/L TCEP, 1X Roche protease inhibitor cocktail and 5% glycerol) and lysed by sonication. The protein was purified by Ni-NTA chromatography, followed by TEV protease cleavage, then a second Ni-NTA chromatography purification, followed by S-200 size exclusion chromatography. Purified protein was stored in 25 mmol/L HEPES (pH = 7.8), 250 mmol/L NaCl, 1 mmol/L TCEP and 5% glycerol.

Ubiquitin (NP_066289.3) amino acids 1 – 76 was cloned in pET21b expression vector with an N-terminal hexahistidine tag. The protein was expressed in *E. coli* BL21-CodonPlus (DE3)-RIL cells by addition of 0.5 mmol/L IPTG for 16 h at 16°C. Cells were resuspended in lysis buffer (25 mmol/L Tris-HCl (pH = 8), 200 mmol/L NaCl, 1 mmol/L TCEP and 5% glycerol) and lysed by passing through a high-pressure homogenizer at 400 bar once and at 900 bar twice. The protein was purified by Ni-NTA chromatography, followed by S-200 size exclusion chromatography. Purified protein was stored in 20 mmol/L Tris-HCl (pH = 8), 300 mmol/L NaCl, 1 mmol/L TCEP and 5% glycerol.

Fusions tags for the four proteins used were as follows: human PARP14 catalytic domain for enzyme assay was MHHHHHHSSGVDLGTENLYFQS followed by PARP14 fragment 1611-1801, human catalytic domain for SPR assay was MHHHHHHSSGVDLGTENLYFQSNAGLNDIFEAKIEWHE followed by PARP14 fragment 1611-1801, mouse catalytic domain was MHHHHHHSSGVDLGTENLYFQS followed by PARP14 fragment 1627-1817, and human full length protein was MHHHHHHSSGVDLGTENLYFQS followed by PARP14 residues 2-1801. Catalytic domains were expressed in *E. coli* while the full length protein was purified from insect cells. Purification steps were nickel column chromatography followed by size exclusion chromatography. For crystallization and SPR usage of the human catalytic domain proteins, the His6 tag was cleaved using TEV protease prior to size exclusion chromatography, and for SPR, the protein was also biotinylated prior to SEC chromatography. For crystallization, purified, tag-cleaved PARP14 (30 mg/mL, 20 mM HEPES, 200 mM NaCl, 2 mM TCEP, pH 7.5) was incubated with RBN012579 or compound **3** as a mixture with its *cis* isomer at a final concentration of 2 mM (final DMSO concentration of 2%) for 1 h at 4°C. For compound **3** (the *cis* isomer was not observed in the crystal), the protein ligand complex was crystallized via vapor diffusion using the sitting drop method at 18°C from the following well conditions: 0.6 M ammonium sulfate, 0.1 M MES pH 6.5, 10% v/v Jeffamine M-600 using a drop size of 0.5 μL reservoir solution and 0.5 μL well solution. Crystals appeared after 5 days. For RBN012759, the protein ligand complex was crystallized via vapor diffusion using the sitting drop method at 18°C from the following well conditions: 0.2 M ammonium sulfate; 0.1 M tri-sodium citrate pH 5.6; 25% w/v PEG 4000 using a drop size of 0.3 μL reservoir solution and 0.3 μL well solution. Crystals appeared after 7 days. The structure of compound **2** was solved by crystal soaking. Crystals were grown by the sitting drop method above and 2-methyl-1,5,6,7-tetrahydro-4H-cyclopenta[4,5]thieno[2,3-d]pyrimidin-4-one, which can be purchased commercially from Aldrich. The well conditions were 0.2 M lithium nitrate, 14% w/v PEG 3350. After formation, crystals were soaked in well solution containing 5 mM compound **2** for 24 h. Crystals were cryoprotected in a solution containing 80% mother liquor and 20% glycerol prior to vitrification in liquid nitrogen. Data reduction and scaling was performed using XIA (compound **2**), HKL3000 (compound **3**), and XDS (RBN012759). Structure determination was performed by molecular replacement utilizing Phaser program from the CCP4 software package. After manual ligand placement, iterative cycles of refinement and model building were performed using REFMAC5 and COOT, respectively. There were no Ramachandran outliers. The crystal structures have been depos-

ited into the Protein Data Bank with PDB codes 6WE4, 6WE3, and 6WE2 for compound **2**, compound **3**, and RBN012759, respectively. Data collection and refinement statistics are shown in [Table S3](#).

Human PARP14 catalytic domain *in vitro* active site probe displacement (TR-FRET) assay

Displacement of a biotinylated small molecule probe from the NAD⁺-binding site of human PARP14 catalytic domain was measured *in vitro* using a TR-FRET assay. A Mosquito (STP Labtech) was used to add 20 nL of a dose response curve of each test compound in DMSO into black 384-well polystyrene Proxiplates (Perkin Elmer), and positive control wells contained RBN010860 and negative control wells contained DMSO (final concentration, f.c. = 0.2%). A Multidrop Combi (Thermo Fisher) was used to add the rest of the reagents. Reactions were performed in an 8 μ L volume by adding 6 μ L of PARP14 catalytic domain (f.c. = 6 nM) and probe (f.c. = 2 nM) in 1X assay buffer (20 mM HEPES pH = 8, 100 mM NaCl, 0.1% bovine serum albumin, 2 mM DTT and 0.002% Tween20), incubating with test compound at 25°C for 30 min, then adding 2 μ L of ULIGHT-anti 6xHis (f.c. = 10 nM) and LANCE Eu-W1024 labeled streptavidin (f.c. = 0.25 nM). Binding reactions were equilibrated at 25°C for an additional 60 min, then read on an Envision plate reader equipped with a LANCE/DELFI top mirror using excitation = 320 nm and emission = 615 nm and 665 nm with a 90 μ s delay (Perkin Elmer). The ratio of the 665/615 nm emission was calculated for each well to determine the relative amounts of complex of PARP14 and the probe formed in each well.

Human full-length PARP14 self-modification enzymatic activity (DELFI) assay

Inhibition of full-length human PARP14 enzymatic activity was performed using an assay format that has been previously described for PARP-monoenzymes (Wigle et al., 2019). Reactions were performed in a 25 μ L volume in 384-well white polystyrene Ni-NTA coated microplates at 25°C. 1X enzyme assay buffer was 20 mM HEPES (pH = 7.5), 100 mM NaCl, 2 mM DTT, 0.1% DTPA-purified BSA and 0.002% Tween 20. Compounds were stored in 100% DMSO and 0.5 μ L were dry-spotted into the microplates. Uninhibited control wells contained DMSO (f.c. = 2%) and fully inhibited control wells contained RBN010860 (f.c. = 200 μ M). His-tagged PARP14 was added in a 20 μ L volume (f.c. = 10 nM) to the microplates and incubated for 30 min before the addition of 5 μ L of biotinylated-NAD⁺ (f.c. = 3 μ M) to initiate the enzymatic reaction. The reaction was stopped after 3 h by addition of 5 μ L of NAD⁺ (f.c. = 2 mM) to outcompete the incorporation of biotinylated-NAD⁺. Quenched reactions were washed five times using 100 μ L of Tris-buffered saline + Tween 20 (TBS-T), followed by addition of 1:1000 DELFIA Eu-N1 streptavidin diluted in DELFIA assay buffer, then incubated for 30 min at 25°C to allow the streptavidin to bind to the incorporated biotin. Next, the reactions were washed five times with 100 μ L TBS-T, followed by addition of 25 μ L of DELFIA enhancement solution. Microplates were incubated 15 minutes, then the DELFIA signal was read on an Envision plate reader (excitation = 340 nm, emission = 615 nm).

Mouse catalytic domain PARP14 *in vitro* active site probe displacement (TR-FRET) assay

Displacement of a biotinylated small molecule probe from the NAD⁺-binding site of mouse PARP14 catalytic domain was measured *in vitro* using a TR-FRET assay similar to the one used for human catalytic domain PARP14, with the following final concentrations: PARP14 = 10 nM, probe = 50 nM, ULIGHT-streptavidin = 4 nM and LANCE Eu-W1024 Anti-His6 = 1 nM.

PARP14 SPR assay

Biotin-Avi-His-TEV-PARP14¹⁶¹¹⁻¹⁸⁰¹ was diluted into running buffer (50 mM HEPES (pH = 7.5), 50 mM NaCl, 1 mM TCEP, 0.05% Tween20 and 2% DMSO) at a concentration of 1 μ M and immobilized to a level of \sim 2000 RU on a streptavidin sensor chip in a Biacore T200 (GE Life Sciences; Marlborough, MA) using a flow rate of 10 μ L/min. Residual streptavidin binding sites were blocked with an injection of PEG-biotin (Thermo Scientific; Waltham, MA) for 2 min at a flow rate of 10 μ L/min and a reference channel blocked with PEG-biotin was also produced in parallel. RBN012759 binding was analyzed using single-cycle kinetics at a flow rate of 80 μ L/min using an association times of 150 s, dissociation times of 300 s between injections, and a final dissociation time of 1800 s. Following subtraction of blank and solvent correction, data was analyzed using single-cycle kinetics fitting via Biacore software.

Human PARP14 catalytic domain thermal shift assay (TSA)

Stabilization of the PARP14 catalytic domain by compound binding was measured using a thermal shift assay in a LightCycler 480 II (Roche). Reactions proceeded in a 15 μ L volume in thermal shift assay buffer (20 mM HEPES pH = 7.5 and 100 mM NaCl). PARP14 (f.c. = 3 μ M) and dye (1X final concentration) were incubated with 0.5 μ L of compound (f.c. = 167 μ M) stored in DMSO (f.c. = 3%) for 30 minutes at 25°C. The assay plate was sealed with an optically clear seal and heated on the LightCycler 480 II with a temperature ramp of 0.11°C/s. The melting temperature (T_m) was determined using the first derivative function and ΔT_m was calculated by subtracting the T_m of PARP14 + RBN012759 from PARP14 + DMSO.

PARP14 NanoBRET cellular biophysical assay

Displacement of RBN01198 binding to NanoLuc-tagged PARP-monoenzyme was measured in live cells using a bioluminescence resonance energy transfer (NanoBRET) assay. A PARP14 expression plasmid was created by inserting a truncated form of PARP14 (1611-1801) into pc DNA3.1(-) vectors coding for N-terminal NanoLuc fusion. The plasmid was prepared for transfection by diluting in OptiMEM +6% FuGENE HD and adding empty vector. A volume of 2.4 mL of diluted plasmid was added to 2×10^7 293T cells, incubated for 24 h under standard growth conditions and then used in the NanoBRET assay. Transfected cells were resuspended in phenol-red free OptiMEM to a concentration of 5×10^5 cells/mL and the NanoBRET probe was added. Next, 40 μ L of cells were

added to white polystyrene 384-well non-binding surface microplate (Corning) using a Multidrop Combi and 40 nL of a dose response curve of each test compound in DMSO was added to the cell plate using a Mosquito. The plate was incubated in a 5% CO₂ environment at 37°C for 2 h, then 20 μL per well of a solution consisting of a 1:166 dilution of NanoBRET substrate (Promega) and a 1:500 dilution of NanoLuc extracellular inhibitor (Promega) in phenol-red free OptiMEM was added to each well. Filtered luminescence was measured on an Envision plate reader equipped with a dual 585 nm mirror, 460 ± 40 nm bandpass filter (donor) and 610 ± 50 nm longpass filter (acceptor) (Perkin Elmer). Experiments were repeated at least three times.

Human primary macrophage culture

Human PBMCs (sex of sample not available) were isolated from a Leukopak® (STEMCELL Technologies) by diluting with an equal volume of EasySep™ buffer (STEMCELL Technologies), gently mixing, and spinning at 120 g for 10 minutes at room temperature. The cell pellet was dislodged, washed in EasySep™ buffer twice, and centrifuged as described above. Red blood cells (RBC) were lysed with ammonium chloride solution (STEMCELL Technologies) according to the manufacturer's instructions. After RBC lysis, PBMCs were resuspended into fresh EasySep™ buffer for counting and again resuspended at 5.0 × 10⁷ cells/mL. Monocytes were isolated from the PBMC cell suspension with the EasySep™ human monocyte isolation kit (STEMCELL technologies) according to the manufacturer's instructions. Monocytes were resuspended in ImmunoCult macrophage media (STEMCELL technologies) containing 50 ng/mL human recombinant M-CSF (STEMCELL technologies) and plated in 12-well plates for Western immunoblotting assays (1.0 × 10⁶ cells/well in 1 mL of media) or 6 well plates for RNAseq experiments (2.5 × 10⁶ cells/well in 2.5 mL of media); and allowed to differentiate for 7 days with fresh media and M-CSF (half volume) added on day 4. Macrophages were ready for downstream assays on day 7.

Cytokine and chemokine measurements

IL-10 concentrations in the supernatant of macrophage cultures were determined with the human IL-10 Quantikine ELISA kit (R&D Systems) using the manufacturer's instructions and with 3 biological replicates. For experiments with the KIRC tumor explants, culture supernatants were collected at 24- and 48 h time points for the detection of cytokine concentrations using the Invitrogen™ Luminex™ Cytokine Human 25-Plex Panel. All samples and standards were prepared and assayed following the manufacturer's protocol. The plate was read, and concentrations of each cytokine determined, using the BioRad® BioPlex™ MAGPIX multiplex reader system.

Immunoblotting

RAW264.7 or CFPAC-1 cells were plated at a density of 4.0⁵ × 10 cells/well in 12-well dishes one day prior to treatment and allowed to adhere overnight. The next day, cells were serum starved for 24 h in 0.1% FBS and subsequently treated with the indicated concentrations of compounds (RBN012759, compound 4, or Niraparib (AdooQ Bioscience) using DMSO as the vehicle (0.1% final concentration in each well) 6 h prior to stimulation with 20 ng/mL mouse IFN-γ (Peprotech) for an additional 24 h. Cells were rinsed with PBS on ice prior to being scraped in 150 μL of 1× radioimmunoprecipitation assay (RIPA) lysis buffer supplemented with 0.1% sodium dodecyl sulfate and 1× Halt™ Protease and Phosphatase Inhibitor Cocktail (Thermo Fisher Scientific). Clarified lysates were assayed for protein concentration by Pierce BCA assay according to the manufacturer's instructions. To run Western blots, 30 μg of protein in sample buffer (LI-COR) were loaded per lane on 18-well 4-12% Bis-Tris gels (Bio-Rad) and run in 3-(N-morpholino)propanesulfonic acid (MOPS) buffer. Gels were transferred to polyvinylidene difluoride (PVDF) membranes using a dry transfer device (Bio-Rad). At completion of transfer, blots were rinsed with water before blocking in Odyssey blocking buffer (LI-COR) and rocking for 1 h at room temperature. Blots were then incubated with primary antibody diluted in blocking buffer overnight at 4°C. The next day, blots were rinsed three times with 2-amino-2-hydroxymethylpropane-1,3-diol (TRIS) buffered saline with Tween-20 (TBST) prior to incubation with secondary antibody diluted in blocking buffer and rocking at room temperature for 45 minutes. Finally, blots were rinsed three times with TBST before imaging on an Odyssey CLx (LI-COR). Analysis was performed with Odyssey Image Studio (LI-COR). Polarized M2-like human macrophages were lysed and processed in the same manner as described above. For the spleen tissue samples, frozen spleen tissue was sectioned on a cold surface with a clean scalpel and homogenized in T-PER (Thermo Fisher Scientific) lysis buffer containing 1x HALT inhibitor and 1 μL/mL benzonase (Sigma-Aldrich). The homogenized lysate was incubated on ice for 15 minutes and centrifuged at 30,000 at 4°C for 15 minutes. Cleared supernatants were further processed as described above. Experiments were repeated at least two times.

NanoString Assay and analysis

KIRC tumor explants were cultured as described below in the explant tumor section. Total RNA was isolated from tumor explants using TRIzol™ Reagent (Thermo Fisher Scientific) following the manufacturer's protocol. After final isolation steps, the RNA pellet was resuspended in warm (37°C) diethyl pyrocarbonate (DEPC)-treated water. The amount of isolated RNA was quantified using the Invitrogen™ Qubit™ 3 Fluorometer (Thermo Fisher Scientific) and stored at -80°C for additional analyses. Total RNA was loaded on a custom 100 gene NanoString array (Canopy Biosciences) (see list below). The NanoString raw data was normalized using nSolver software. Expression changes for each gene and tumor treatment condition were calculated by the log-transformed ratio between compound treated and DMSO-treated sample values. The expression change profiles were characterized using a heatmap with a k-means clustering of the gene changes (k = 3) and hierarchical clustering of samples specifying the order of rows and columns, respectively (R package ComplexHeatmap (v2.2.0)). The following additional genes were added to the panel and include:

APP, CTSA, CTSB, CTSC, CTSD, EPHA2, EPHB1, EREG, HLA-DQB2, IL3RA, KYNU, LY75, LYVE1, MMP14, MSR1, NRP2, PARP1, PARP10, PARP11, PARP14, PARP15, PARP16, PARP2, PARP3, PARP6, PARP8, PLAUR, TIPARP, TNKS2, and ZC3HAV1.

RNA sequencing and analysis

Human primary macrophages were cultured as referenced above and plated at a density of 1.0×10^6 cells/well in 1 mL of macrophage media in 6-well dishes. Macrophages were treated with 1 μ M or 0.1 μ M of compound 6 h prior to stimulation with 15 ng/mL of IL-4 (M2) or IFN- γ (M1) or left in the naïve condition for an additional 18 h. Sample set up included 3 biological replicates per condition. Samples were collected 6 h and 18 h post stimulation by lysing and scraping in 350 μ L/well of TRIzol™ Reagent. RNA was isolated with QIAshredder columns (QIAGEN) and the Mag MAX kit (Ambio) according to the manufacturer's instructions. RNA sequencing was performed at the BioMicroCenter at MIT with a single lane of an Illumina NextSeq. Illumina software produced the raw, de-multiplexed sequencing intensity files.

Transcriptome sequences were mapped and quantified using Salmon software (v0.11.26). The mapping-based mode with a GenCode (release 29) human reference transcriptome index was used for alignment. To characterize the sequenced samples based on their measured whole-transcriptome profiles, hierarchical clustering was performed using a Poisson distance metric (R package Poi-ClaClu (v1.0.2.1)(Witten, 2011)). Transcriptome read counts for each sequenced sample were then analyzed to identify differentially expressed genes using R package DESeq2 (v1.18.17). Comparisons were made between PARP14 inhibitor-treated samples with and without IL-4 stimulation and untreated samples with and without stimulation. The genes with significant expression changes (multiple testing adjusted p-values < 0.05 and an absolute log₂ fold-change > 2) in either the vehicle with IL-4 stimulation compared to vehicle and no stimulation comparison, or the PARP14 inhibitor treatment with IL-4 stimulation compared to vehicle with IL-4 stimulation were extracted and their expression values normalized against the mean of the vehicle with no stimulation expression values. A k-means clustering (k = 5) of the normalized expression values and heatmap visualization were performed with R package ComplexHeatmap (v2.2.0).

Substrate identification

Cell lysis, immunoprecipitation, and mass spectrometry analysis methods have been described(Lu et al., 2019). In short, IFN- γ -treated human primary macrophages were treated with DMSO or 10 μ M compound 4 for 48h. ADP-ribosylated proteins were immunoprecipitated using Af1521-conjugated magnetic resin (Tubip BioLabs). After incubation for 1 h at 4°C, the resin was washed 3 times in PBS followed by elution in 100 μ L of 1X sample loading buffer at 65°C for 5 min. Af1521 immunoprecipitation eluates were submitted to MS Bioworks (Ann Arbor, MI) for mass spectrometric sample preparation and analysis(Lu et al., 2019).

The detected proteins and their corresponding spectral counts were compared to the genes with opposing expression changes with and without PARP14 inhibitor treatment in the IL-4 stimulation setting. The comparison between these sets was performed at the gene set level, whereby overlapping enriched gene sets from the two datasets were identified. For the substrate identification dataset, all the proteins with a reduction in spectral count in the treated sample compared to the untreated sample were input into an enrichment analysis with Gene Ontology gene sets using R package clusterProfiler (v3.14.0) (Yu et al., 2012). The enrichment analysis is based on a hypergeometric test to determine over- or under-represented gene sets among the input list of proteins. The same enrichment analyses were performed with significant opposing expression effects genes (adjust p-value < 0.05). For PARP14 immunoprecipitation, 10 μ g of PARP14 antibody was conjugated to 100 μ L of Protein G Dynabeads (Thermo Fisher Scientific) according to manufacturer recommended protocol. Two mg of CFPAC-1 lysate from cells treated with or without 1 μ M RBN012759 followed stimulation with or without 20 ng/mL human IFN- γ were incubated with resin for 1 h at 4°C. After washing, proteins were eluted by incubating resin with sample buffer (LI-COR) for 5 min at 65°C then separated on 4–20% TGX polyacrylamide gels (Bio-Rad). Proteins in the gel were transferred to a piece of Immobilon-FL PVDF membrane (EMD Millipore) using the TransBlot Turbo (BioRad) semi-dry transfer setup. The membrane was blocked in TBS Odyssey Blocking Buffer (LI-COR) for overnight, followed by incubation with primary antibody and the QuickWestern detection reagent (LICOR) for 2 h at room temperature. After washing with TBS-T, the blot was scanned on the Odyssey CLx infrared imaging system (Lu et al., 2019).

Human tumor explant culture and RNA extraction

The human tumor explants were grown as previously described (Page et al., 2018; Mediavilla-Varela et al., 2018). Briefly, procedures were carried out at Niloten Oncosystems. Tumor samples (sex of patients from which tumoroids were made from is not available) were obtained with informed consent and relevant IRB approval from patients with renal cell carcinoma. Fresh tumors were processed into tumoroids of approximately 150 microns in size using a proprietary method, and approximately 400 tumoroids from each individual tumor were pooled in culture plates. Tumoroids were treated as referenced in Figure 5A for 24h. Total RNA was isolated from tumor organoids by using the TRIzol™ Reagent (Invitrogen) following the manufacturer's protocol. After final isolation steps, the RNA pellet was resuspended in warm (37°C) Diethyl pyrocarbonate (DEPC)-treated water (Quality Biological). The amount of isolated RNA was quantified using the Invitrogen™ Qubit 3™ Fluorometer (Thermo Fisher Scientific) and stored at -80°C for additional analyses.

TCGA analysis

TCGA gene expression data were extracted from Genomics Data Commons Portal using the HTSeq – Counts workflow analysis (<https://portal.gdc.cancer.gov>). Tumor immune cell infiltrate and purity estimates were obtained from the TIMER resource(Li et al.,

2016). R packages survminer (v0.4.3) and RTCGA (v1.10.0, clinical and rna-seq 20160128) were used to perform the survival-expression analyses. Specifically, survival curves were compared for “high” and “low” PARP14 expression level groups, defined by the maxstat R package (v0.7.25).

In vivo pharmacokinetics and bioanalysis

51 mg RBN012759 was dissolved into 1.0 mL 0.5% methylcellulose and 0.2% Tween 80 in water with vortexing, sonicating and stirring at room temperature for 20 min to obtain a homogenous suspension with a concentration of 50 mg/mL. The formulated compound (500 mg/10mL/kg) was dosed slowly via oral gavage to $n = 3$ male CD-1 mice. 0.03 mL blood was collected at each time point via submandibular bleed. Each sample was transferred into plastic microcentrifuge tubes containing Heparin-Na and mixed well, then placed on wet ice prior to centrifugation. Samples were centrifuged at 4000 g for 5 min at 4°C to obtain plasma and stored at $-75 \pm 15^\circ\text{C}$ prior to analysis.

RBN012759 compound levels were determined by HPLC-MS/MS analysis. A stock solution of RBN012759 was prepared at 1 mg/mL in DMSO. For undiluted plasma samples, an aliquot of 30 μL sample was added to 200 μL internal standard (dexamethasone, 50 ng/mL) in acetonitrile. The mixture was vortexed for 5 min at 750 rpm and centrifuged 14,000 rpm for 5 min. An aliquot of 5.0 μL supernatant was injected for LC-MS/MS analysis. For diluted plasma samples, an aliquot of 10 μL and 3 μL sample was added with 20 μL and 27 μL of blank plasma for 3-fold and 10-fold dilutions, respectively. For 50-fold diluted samples, an aliquot of 2 μL sample was first added with 8 μL of blank plasma. After vortexing for 5 min at 750 rpm an aliquot of 3 μL of diluted sample was added with 27 μL of blank plasma for second step dilution. The diluted samples were added to 200 μL internal standard (dexamethasone, 50 ng/mL) in acetonitrile. The mixture was vortexed for 5 min at 750 rpm and centrifuged at 14,000 rpm for 5 min. An aliquot of 5.0 μL supernatant was injected for LC-MS/MS analysis.

In vivo target engagement

C57Bl/6 J female mice were obtained from the Shanghai Lingchang BioTech Co., Ltd and kept in individual ventilation cages with free access to food and water at constant temperature and humidity with 3 or 5 animals in each cage. Mice were between 6 to 8 weeks of age. Mice were administered vehicle by oral gavage twice a day (BID) for 5 days or either 300 or 500 mg/kg of RBN012759 by oral gavage twice a day (BID) for 7 days. RBN012759 was dissolved in 0.5% methylcellulose (Sigma-Aldrich) + 0.2% Tween 80 (Sigma-Aldrich). Each dose was delivered in a volume of 0.2 mL/20 g mouse (10 mL/kg) and adjusted for the last recorded weight of individual animals. Mice were monitored and body weight was measured daily. Plasma was collected at 2 and 12 h after the first or the last dose. Spleen tissues were collected at 12 h after the last dose and stored at -80°C until further analysis, described in the Immunoblotting method above.

QUANTIFICATION AND STATISTICAL ANALYSIS

In general, data were analyzed in Excel or Prism. Details of replicates and data analysis for each experiment can be found in the figure legends or methods section.

% Inhibition

The % inhibition for all assays was calculated as shown below:

$$\% \text{ inhibition} = 100 \times \frac{\text{signal}_{\text{cmpd}} - \text{signal}_{\text{min}}}{\text{signal}_{\text{max}} - \text{signal}_{\text{min}}}$$

where $\text{signal}_{\text{cmpd}}$ is the assay signal from the compound treated well, $\text{signal}_{\text{min}}$ is the assay signal from the positive control well and $\text{signal}_{\text{max}}$ is the assay signal from the DMSO-treated negative control well.

IC₅₀ curve fitting

The % inhibition values were plotted as a function of compound concentration and the following 4-parameter fit was applied to derive the IC₅₀ values:

$$Y = \text{Bottom} + \frac{(\text{Top} - \text{Bottom})}{\left(1 + (X/\text{IC}_{50})^{\text{Hill Coefficient}}\right)}$$

Typically, the 4-parameters were allowed to float, however in some cases the bottom or top of the curves were fixed at 0% or 100% respectively. IC₅₀ data reported as geometric means throughout the manuscript, and geometric means \pm standard deviations and number of experiments is listed in the [supplemental information](#).

Pass/fail criteria for screening plates

Plates were failed if the Z' (Zhang et al., 1999) was below 0.5, as well as if the IC₅₀ value for a reference inhibitor included on each plate did not register to within 3-fold of its historical averaged IC₅₀.